



Active Spreading: Hydraulics for Enhancing Groundwater Remediation

Lauren J. Sather, Ph.D.¹; Roseanna M. Neupauer, Ph.D., P.E., M.ASCE²; David C. Mays, Ph.D., P.E., M.ASCE³; John P. Crimaldi, Ph.D.⁴; and Eric J. Roth, Ph.D.⁵

Abstract: During in situ groundwater remediation, reactions occur in a narrow reaction front in which the amendment and contaminant are close enough to mix. Active spreading, in which injection or extraction wells create spatially variable velocity fields, can be used to increase the surface area of the reaction front, thereby enhancing reaction. This study used four active spreading flow fields that are building blocks to more complex remediation hydraulics to evaluate how the flow field and the plume position control contaminant degradation in both homogeneous and heterogeneous aquifers. At the plume scale, reaction depended on mechanical dispersion across the reaction front, which is proportional to both the local velocity and the local contaminant concentration gradient. Mechanical dispersion and, consequently, the amount of degradation, was highest when the reaction front was perpendicular to the local velocity, producing a high local dispersion coefficient. This effect was amplified where flow was diverging due to sharpening of the concentration gradient. DOI: 10.1061/(ASCE)HE.1943-5584.0002167. © 2022 American Society of Civil Engineers.

Introduction

In situ remediation is a common method for cleaning up contaminated groundwater. During in situ remediation, a chemical or biological amendment is introduced into an aquifer to react with and degrade a contaminant. Reaction between the amendment and the contaminant take place only within a relatively narrow region, called the reaction front, in which the contaminant and amendment are sufficiently close to react. Degradation reactions along the reaction front are controlled by spreading and mixing. Mixing involves the smoothing of concentration gradients by molecular diffusion and pore-scale dispersion (Bellin et al. 2011), which brings molecules together to react. Spreading involves the reconfiguration of the contaminant and amendment plumes as a result of spatial variations in velocity (Le Borgne et al. 2010). Spreading enhances mixing by sharpening the concentration gradient and elongating the interface along which mixing can occur (Le Borgne et al. 2013). It is helpful to distinguish between passive spreading and active spreading. Passive spreading results from velocity variations caused by aquifer heterogeneity, while active spreading results from induced velocity variations (e.g., by injecting or withdrawing water through wells).

The key to successful in situ remediation is to deliver the amendment in such a way that the reaction front is spread throughout the

Note. This manuscript was submitted on April 30, 2021; approved on January 11, 2022; published online on March 10, 2022. Discussion period open until August 10, 2022; separate discussions must be submitted for individual papers. This paper is part of the *Journal of Hydrologic Engineering*, © ASCE, ISSN 1084-0699.

contaminant plume. The most basic method of amendment delivery is to install a well in the plume, typically where contaminant concentrations are highest, through which the amendment is injected. Then, the contaminant and amendment plumes are left to travel through the subsurface under natural hydraulic gradients. The reaction front is reconfigured by passive spreading due to aquifer heterogeneity, which may elongate the reaction front, thereby creating more contact between the contaminant and amendment (Le Borgne et al. 2013, 2014; Bandopadhyay et al. 2017). Passive spreading also increases the concentration gradients at the reaction front, increasing the driving force for mass flux by molecular diffusion and dispersion (Ou and Ranz 1983; Le Borgne et al. 2013). Although passive spreading enhances reaction to some degree, large portions of the amendment plume may remain isolated from the contaminant plume; consequently, the delivery of the amendment into the contaminant plume is incomplete.

Most in situ remediation installations rely on the use of injection and extraction wells to enhance delivery of the amendment and to direct the movement of the amendment through the contaminated area. Injection and extraction wells can be used in pairs (dipoles) for smaller plumes, in multiwell cells, or in multiple groups of multiwell cells for large plumes (Suthersan et al. 2009). More advanced in situ remediation designs reconfigure the active spreading flow fields during the remediation process; this has been shown to further enhance remediation (Suthersan et al. 2015). In these active spreading systems, the reaction front is reconfigured as imposed flow forcings from the injection and extraction wells create spatially variable velocity fields (Zhang et al. 2009; Lester et al. 2010; Trefry et al. 2012; Mays and Neupauer 2012; Suthersan et al. 2015). As with passive spreading, active spreading elongates the reaction front and increases concentration gradients along the reaction front; this has been shown to enhance mixing (Le Borgne et al. 2010) and reaction (Piscopo et al. 2013; Bandopadhyay et al. 2017; Rodríguez-Escales et al. 2017; Cho et al. 2019).

While active spreading has been shown to enhance reaction during in situ remediation, the nature of the causal relationships between active spreading flow fields, the geometry of the reaction front, and the degree of enhanced mixing-controlled reaction in porous media are not well understood. To design remediation systems that most

¹Scientist II, West Yost Associates, Lake Forest, CA 92630. Email: lauren.reising@colorado.edu

²Professor, Univ. of Colorado Boulder, 1111 Engineering Dr., UCB 428, Boulder, CO 80309-0428 (corresponding author). ORCID: https://orcid.org/0000-0002-4918-810X. Email: neupauer@colorado.edu

³Professor, Univ. of Colorado Denver, Campus Box 113, P.O. Box 173364, Denver, CO 80217-3364. ORCID: https://orcid.org/0000-0002-5218-1670

⁴Professor, Univ. of Colorado Boulder, 1111 Engineering Dr., UCB 428, Boulder, CO 80309-0428.

⁵Postdoctoral Fellow, Univ. of Colorado Anschutz Medical Campus, Aurora, CO 80056.

effectively capitalize on the spatiotemporal variations in spreading and mixing conditions, an investigation into the relationship between active spreading and mixing-controlled reaction under flow fields typical of remediation systems is necessary. Accordingly, the goal of this study was to evaluate how active spreading at the plume scale impacts the overall degradation of a contaminant plume.

Several studies have investigated spreading, mixing, and reaction at scales much smaller than the plume scale. A subset of studies considered situations in which one species is invading a region occupied by another; thus, the reaction front is approximately perpendicular to the local velocity vectors. Due to pore-scale velocity variations and incomplete mixing in the pore space, spreading occurs as the invading species forms lamellae within the pore (Le Borgne et al. 2013),

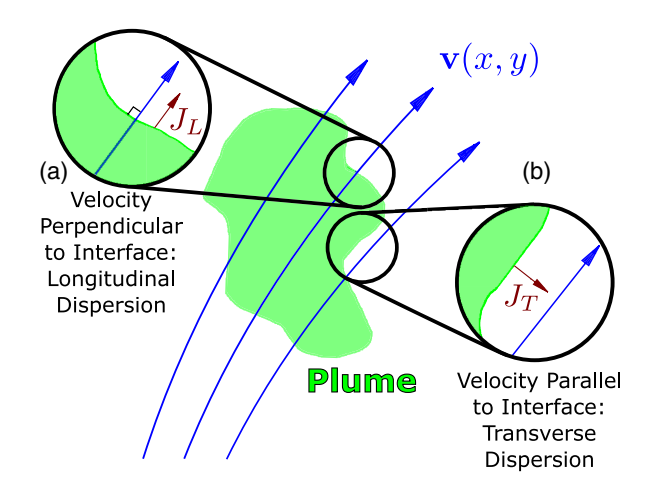


Fig. 1. Schematic of plume and local velocity field: (a) location with purely longitudinal dispersive mass flux, J_L ; and (b) location with purely transverse dispersive mass flux, J_T .

which elongates the fluid interface and sharpens the concentration gradients that drive diffusive mixing and reaction. The relationship between lamella formation and diffusive mixing and reaction has been studied in uniform flow with passive spreading (Chiogna et al. 2012; de Anna et al. 2014; Le Borgne et al. 2014; Perez et al. 2020), shear flow (Le Borgne et al. 2014; Bandopadhyay et al. 2017), stratified random flow (Le Borgne et al. 2014), and radial flow (Le Borgne et al. 2014). While radial flow falls under the category of active spreading, it is a special case in which the bulk velocity is everywhere perpendicular to the plume interface on the macroscale. In cases in which one species invades another at the plume scale [as shown in Fig. 1(a)], lamella formation at the pore scale underpins the upscaled process of longitudinal dispersion, with dispersion length scales that have been shown to increase with time at a rate that depends on the heterogeneity of the porous medium (Le Borgne et al. 2013; Perez et al. 2020).

Several other studies have investigated spreading, mixing, and reaction in which the reaction front is approximately parallel to the local velocity vector [as shown in Fig. 1(b)]. This reaction front geometry forms from a continuous point release of a solute (Rolle et al. 2009; Chiogna et al. 2011, 2012) that grows into an elongated plume with high concentration gradients and a long interface parallel to flow such that reactions depend on transverse dispersion. A related study considered transverse dispersion between two adjacent solute plumes with the interface aligned in the main flow direction (Cirpka et al. 2011). Mixing and reaction were enhanced by the spatial variability in velocity caused by spatially segregated high permeability zones (Rolle et al. 2009) or small-scale heterogeneity (Cirpka et al. 2011), while temporal variations in uniform flow had little effect (Rolle et al. 2009).

These previous studies of spreading, mixing, and reaction have considered flow fields and plume configurations in which the orientation of the plume boundary is either perpendicular to or parallel to the direction of the bulk flow. During in situ remediation, an amendment plume (species B in Fig. 2) is emplaced within a

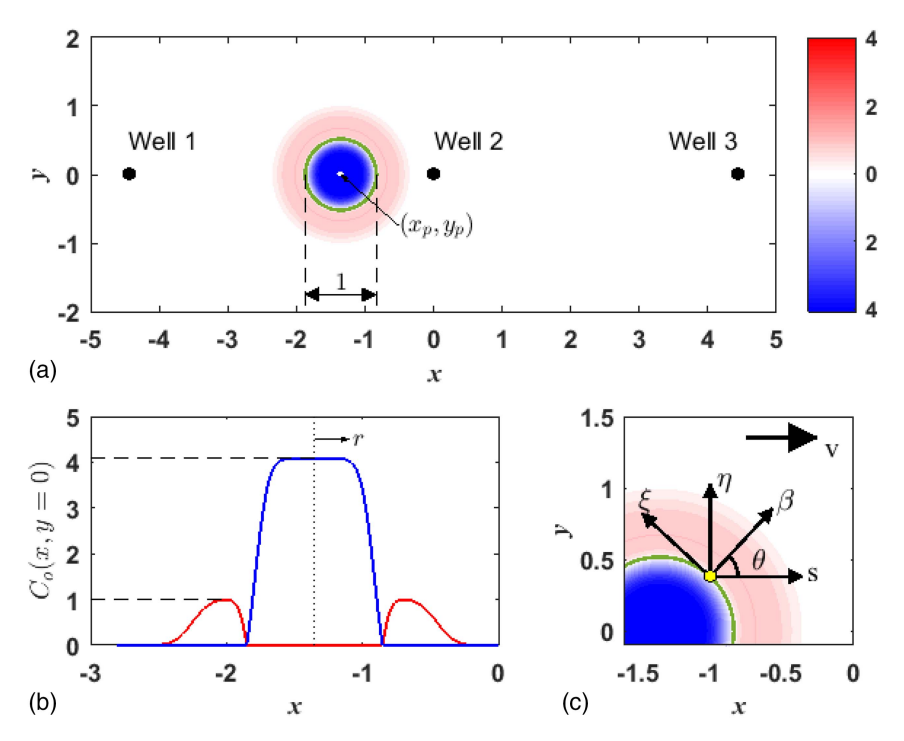


Fig. 2. Initial concentration distributions of species A (outer plume) and B (inner plume): (a) plan view; (b) slice through y = 0; and (c) enlargement showing vectors representing the direction locally perpendicular to the reaction front β , the local flow direction s, the direction locally tangential to the reaction front ξ , and the direction transverse to local flow η from an arbitrary point (open dot), assuming uniform flow in the x-direction.

contaminant plume (species A in Fig. 2), with the reaction front represented by the interface between the two plumes. Because the amendment plume and reaction front are finite in size, the orientation of the reaction front relative to the local velocity varies along the reaction front between the two previously investigated end-member orientations (perpendicular and parallel to flow). Furthermore, under active spreading flow fields, the reaction front experiences different local velocities over time as it travels through the spatially varying velocity field. Therefore, an individual segment of the reaction front will experience different orientations relative to the local velocity in time. This temporally varying local orientation of the reaction front relative to the local flow direction has not been considered in previous studies of spreading, mixing, and reaction. In these more complicated active spreading flows, the local orientation of the reaction front relative to the local flow direction varies both spatially and temporally, leading to spreading and mixing conditions that evolve over time. Therefore, local details drive plume-scale reaction.

In this study, we investigated the relative importance of the two orientations of the reaction front relative to the local velocity and the spatiotemporal variation of these relative orientations in promoting reaction during in situ remediation of contaminated groundwater. Understanding how the local geometries of the reaction front and the flow field control the amount of reaction will enable design of active spreading protocols that exploit local efficiencies to increase the overall amount of degradation during in situ remediation. We considered the plume scale and focused on the continuum behavior over the Darcy and larger scales, because that is the scale of interest in groundwater remediation activities. While several studies have shown that incomplete mixing in pores limits reaction (Gramling et al. 2002; Raje and Kapoor 2000), the errors associated with neglecting incomplete mixing at the Darcy and larger scales may be negligible for the fast reactions considered in this study (Porta et al. 2013).

In this study, we derived an explicit relationship between the global reaction rate, quantified for the plume as a whole, and local characteristics of the plumes and velocity field along the reaction front. We applied this relationship to four different active spreading protocols that represent components of flow fields that may be used to drive flow during in situ remediation, and we compared the results to uniform flow (i.e., no active spreading). Because this study focused on active spreading, we initially removed the effects of passive spreading by considering homogeneous aquifers only. This simplification allowed us to evaluate the features of the flow field alone that promote reaction on the plume scale and to identify patterns of flow and reaction front geometry that produce the most degradation. We evaluated how the topology of the flow field enhances or inhibits the overall degradation of the contaminant. Then, we extended the investigation to heterogeneous aquifers, and we demonstrated that the same patterns of flow and reaction front geometry that produce the most degradation in homogeneous aquifers also generally produced the most degradation in the heterogeneous aquifers we tested. Insights gained from this research will provide crucial information for the optimal design of active spreading groundwater remediation systems in the field.

Reactive Transport Theory

In the first part of this study, we consider a two-dimensional, rectangular, confined, homogeneous isotropic aquifer, centered at the origin. We assume the aquifer contains a circular plume of species A (contaminant) surrounding a circular plume of species B (amendment), as shown in Fig. 2. The chemical reaction between the species follows an instantaneous, irreversible bimolecular reaction,

given by $A+B \rightarrow C$, which can represent, for example, oxidation of chlorinated solvents by potassium permanganate (Yoon and Schwartz 1999). We assume that reactive transport is governed by the advection-dispersion-reaction equation, given by

$$\frac{\partial C_i}{\partial t} = -\nabla \cdot (\mathbf{v}C_i) + \nabla \cdot \mathbf{D}\nabla C_i + R_i \tag{1}$$

where C_i = dimensionless concentration of the *i*th species (i = A, B, C); t = dimensionless time; \mathbf{v} = dimensionless groundwater velocity vector; R_i = dimensionless reaction rate of species i, with $R_A = R_B = -R_C$; and \mathbf{D} = dimensionless dispersion tensor, with components given by

$$D_{xx} = \alpha_L \frac{v_x^2}{|\mathbf{v}|} + \alpha_T \frac{v_y^2}{|\mathbf{v}|} + D_m,$$

$$D_{xy} = D_{yx} = (\alpha_L - \alpha_T) \frac{v_x v_y}{|\mathbf{v}|},$$

$$D_{yy} = \alpha_L \frac{v_y^2}{|\mathbf{v}|} + \alpha_T \frac{v_x^2}{|\mathbf{v}|} + D_m$$
(2)

where α_L and α_T = dimensionless longitudinal and transverse dispersivities, respectively; and D_m = dimensionless molecular diffusion coefficient. The dimensionless velocity comes from the dimensionless form of Darcy's law, given by $\mathbf{v} = -(K/n)\nabla h$, where K is dimensionless hydraulic conductivity, n is porosity, and h is dimensionless head, obtained from

$$\nabla \cdot Kb\nabla h + \sum_{i=1}^{3} Q_{j}\delta(\mathbf{x} - \mathbf{x}_{wj}) = 0$$
 (3)

where b = dimensionless thickness of the aquifer; and Q_j = dimensionless injection rate at well j (Q_j < 0 indicates extraction), located at \mathbf{x}_{wj} . Boundary conditions on Eq. (1) are $\nabla C_i \cdot \mathbf{n} = 0$ on all boundaries, where \mathbf{n} is the outward unit normal vector. The initial condition is shown graphically in Fig. 2. The boundary conditions on Eq. (3) are

$$\frac{\partial h}{\partial y} = 0$$
 at $y = \pm L/2$ (4)

$$h = h_L \quad \text{at} \quad x = -L/2 \tag{5}$$

$$h = 0$$
 at $x = L/2$ (6)

where L= dimensionless length of the domain; and $h_L=$ dimensionless head at the boundary at x=-L/2. For the active spreading scenarios, we assume background flow is negligible, so $h_L=0$; for comparison, we also consider uniform flow (i.e., no active spreading), with $h_L\neq 0$.

All dimensionless lengths are relative to the diameter d of the initially circular reaction front. Because we are considering steady flow, the situation does not have a natural characteristic time. Instead, we define the characteristic time in terms of a characteristic pumping rate, defined as the sum of the magnitudes of all active pumping rates (per unit aquifer thickness). With this characteristic length and pumping rate, the characteristic time is the time required for the characteristic pumping rate to fill a cuboid whose top and bottom surfaces are squares of length d and whose height is equal to the aquifer thickness. Dimensionless concentrations are relative to the maximum concentration of species A in the aquifer at t=0. See Eqs. (S1)–(S4) for the development of the dimensionless forms of the equations.

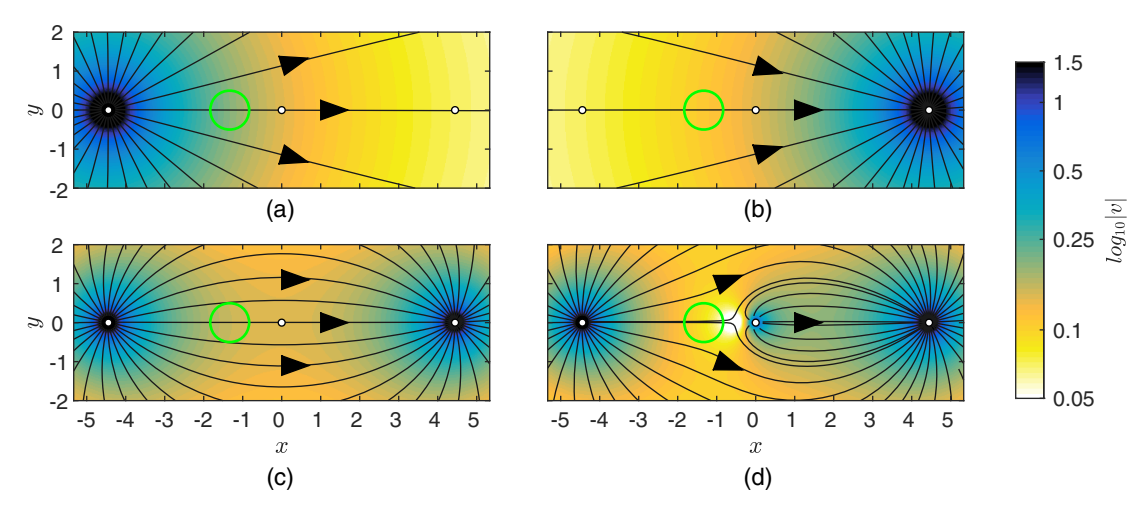


Fig. 3. Velocity field for (a) diverging; (b) converging; (c) dipole; and (d) stagnation active spreading protocols. Black lines are streamlines; arrows show flow direction. White circles are locations of the wells. The circles centered at (x, y) = (-1.33, 0) represent the reaction front at t = 0.

Numerical Model and Active Spreading Protocols

We consider four different active spreading protocols (Fig. 3). The two basic active spreading protocols that we consider are diverging (injection in Well 1) and converging (extracting from Well 3) protocols [Figs. 3(a and b)]. These two protocols can be superimposed in space and time to create more complex active spreading flow fields. The third active spreading protocol is the dipole protocol [Fig. 3(c)], which is the superposition of the diverging and converging protocols. The stagnation protocol [Fig. 3(d)] is similar to the dipole protocol except that the injected water is split between Wells 1 and 2, leading to significant elongation of the reaction front. This protocol is used to evaluate the importance of spreading on reaction. For all four active spreading protocols, ambient flow is assumed negligible, and the amendment and contaminant plumes are initially between Wells 1 and 2 (see plumes in Fig. 2 and reaction front in Fig. 3); thus, the amendment plume is assumed to have been emplaced with a well at (x_p, y_p) that is not shown and not used in the active spreading protocols.

For comparison, we also evaluate a uniform flow field (uniform protocol), which, by definition, exhibits no plume spreading, because spreading is caused by velocity variations, which are absent in uniform flow in a homogeneous aquifer. To make equivalent comparisons across protocols, all protocols except the stagnation protocol are designed to have the same advective travel time between the center of the initial plume $(x_p, y_p) = (-1.33,0)$ and (x, y) = (1.33,0), allowing comparison of protocols across time. For the uniform protocol, this design resulted in a dimensionless velocity higher than typical groundwater flow velocities.

The flow fields for the four protocols and the uniform flow condition were generated by solving Eq. (3) numerically using MODFLOW-2000 version 1.12.00 (Harbaugh et al. 2017). Parameter values for the flow simulations are given in Table 1, and dimensionless pumping rates for each protocol are shown in Table 2.

The reactive transport, Eq. (1), was solved numerically using RW3D version 6.0 (Salamon et al. 2006), which uses random walk particle tracking. Particle tracking is a common method for modeling solute transport in aquifers known for its computational efficiency and absence of numerical dispersion (Berkowitz et al. 2006; Le Borgne et al. 2008a, b). Parameter values are given in Table 1. Instead of solving Eq. (1) directly for species A, B, and C, we simulated the transport of two conservative species, A + C and B + C, eliminating the reaction term in Eq. (1) (Gramling et al. 2002). Assuming a 1:1 mass ratio and a 1:1 stoichiometric ratio

of A and B, the mass concentrations of A, B, and C are obtained from the conservative components as

$$C_C(x, y, t) = \min[2C_{A+C}(x, y, t), 2C_{B+C}(x, y, t)]$$
 (7)

$$C_A(x, y, t) = C_{A+C}(x, y, t) - 0.5C_C(x, y, t)$$
 (8)

$$C_B(x, y, t) = C_{B+C}(x, y, t) - 0.5C_C(x, y, t)$$
 (9)

The initial distributions of concentrations of species A and B were obtained using analytical expressions of transport in radial flow presented in Neupauer et al. (2020). The initial condition is created by injecting fluid at a unit rate at location (x, y) = (-1.33,0).

Table 1. Parameter values in flow and reactive transport simulations

Parameter	Value
Hydraulic conductivity, K	3.57
Aquifer thickness, b	1.78
Porosity, n	0.25
Length of side of square aquifer, L	53.4
Finite-difference grid discretization	0.0222
Head at $x = -L/2$, h_L for active spreading protocols	0
Head at $x = -L/2$, h_L for uniform flow protocol	0.534
Coordinates of Well 1, \mathbf{x}_{w1}	(-4.44, 0)
Coordinates of Well 2, \mathbf{x}_{w2}	0, 0
Coordinates of Well 3, \mathbf{x}_{w3}	(4.44, 0)
Longitudinal dispersivity, α_L	0.0178
Transverse dispersivity, α_T	0.00178
Molecular diffusion coefficient, D_m	0

Note: All values are dimensionless.

Table 2. Dimensionless injection (positive) and extraction (negative) rates for the protocols

Protocol	Injection/extraction pattern		
Name	Well 1	Well 2	Well 3
Diverging	1.0	0	0
Converging	0	0	-1.0
Dipole	0.5	0	-0.5
Stagnation	0.4	0.1	-0.5
Uniform	0	0	0

The injection period was divided into two steps. In the first step of duration of $t_A = 0.466$, the injected fluid contained species A at a dimensionless concentration of 1.02. In the second step of duration $t_R = 0.155$, the injected fluid contained species B at a dimensionless concentration of 4.08. Advection (due to injection), dispersion, and reaction were all simulated during the injection steps. The distributions of species A and B at the end of the injection period are shown in Fig. 2, which corresponds to the initial condition (at t = 0) for all protocols, while the concentration of species C was set to zero everywhere. The maximum dimensionless concentrations of species A and B in the initial plume distribution were 1.00 and 4.08, respectively; and the dimensionless masses of species A and B in the aquifer at time t = 0 were 0.39 and 0.54, respectively. During emplacement of the initial plumes, no flow other than the advection caused by injection of the plumes was present. At time t = 0, the flow for each protocol was initiated and was assumed to immediately attain steady state conditions.

In RW3D, species A + C and B + C were represented as collections of 6×10^6 and 2×10^6 randomly placed particles, respectively, each of which had dimensionless mass of 6.53×10^{-8} and 2.73×10^{-7} , respectively. The smoothness of the concentration distribution depends on the number of particles per unit area. Because the plume of species B covered a smaller area than the plume of species A, fewer particles of species B were used. Relative to the plume centroid at (x_p, y_p) , particle positions in the radial direction were randomly placed to match the distribution in Fig. 2(b), and particle position in the angular direction was drawn from a uniform distribution.

At each output time, the particle positions and masses provided by RW3D were converted to a concentration field by binning the particles into square bins of size 0.0089. Subsequently, the concentration field was smoothed by convolution with a two-dimensional Gaussian distribution with mean zero. The standard deviation of the Gaussian distribution ranged from 0.0089 at early times to 0.3560 at later times. A smaller standard deviation was necessary for early times to avoid oversmoothing the sharp concentration gradients along the reaction front, while a larger standard deviation was necessary for later times, because the area of the plumes increases with time. All analyses and the presentation of the results use the smoothed concentration distributions.

Global and Local Measures of Spreading, Mixing, and Reaction

The metrics used in this paper to quantify spreading, mixing, and reaction include global measures that characterize the behavior of the entire plume and local measures that characterize behavior on scales much smaller than the plume scale. We considered three global measures. Because the purpose of groundwater remediation is to remove a contaminant from an aquifer, the first global measure is the cumulative amount of species A (contaminant) that has reacted, $M_{\rm rxn}$, at or before time t, given by

$$M_{\rm rxn}(t) = M_{Ao} - M_A(t)$$
 (10)

where $M_A(t)$ = dimensionless mass of species A in the domain at time t, calculated as

$$M_A(t) = \iint_{x,y} nC_A(x, y, t) dx dy \tag{11}$$

where $M_{Ao} = M_A(t=0)$ = initial dimensionless mass of species A. Note that Eq. (10) is valid as long as the mass of species A extracted from an active spreading extraction well is minimal. For the

scenarios in this study, less than 2.4% of the mass of species A was extracted in any simulation; we considered this minimal.

The second global measure is the global reaction rate $dM_{\rm rxn}/dt$, which is a measure of the required duration of the remediation. The global reaction rate can be obtained by evaluating the change in $M_{\rm rxn}$ between subsequent time steps of the numerical simulation. Note that it is related to the total mass flow rate of species A (which is equivalent to the mass flow rate of species B) across the reaction front Γ , given by

$$\frac{dM_{\rm rxn}}{dt} = b \oint_{\Gamma} J_{A\beta} d\Gamma \tag{12}$$

where $J_{A\beta}$ = mass flux of species A across the reaction front; and β = direction perpendicular to the reaction front [Fig. 2(c)]. For very fast, irreversible reactions, the reaction front reduces to a surface along which the concentrations of both species vanish; therefore, the advective mass fluxes of both species across the reaction front vanish. Furthermore, if molecular diffusion is negligible (see justification in Fig. S1), $J_{A\beta}$ represents the dispersive mass flux in the β direction.

The third global measure is the reaction front length, L_{Γ} , which is a measure of spreading. This measure allowed us to evaluate the overall importance of spreading during in situ remediation.

We used local measures to quantify how local characteristics of the plume, reaction front geometry, and the velocity field affect contaminant degradation. As shown in Eq. (12), the global reaction rate is controlled by the local dispersive mass flux $J_{A\beta}$ of species A across the reaction front, given by

$$J_{A\beta} = -nD_{\beta} \frac{\partial C_A}{\partial \beta} \tag{13}$$

where D_{β} = dispersion coefficient in direction β ; and $\partial C/\partial \beta$ = concentration gradient of species A in direction β . Therefore, we identify $J_{A\beta}$, D_{β} , and $\partial C/\partial \beta$ as three local measures of mixing.

These local mixing measures can be evaluated by equating $J_{A\beta}$ with its components in the direction of local velocity vector s and in the direction perpendicular to local velocity vector η [Fig. 2(c)]. The local dispersive mass fluxes in the s- and η -directions are, respectively

$$J_{As} = -n\alpha_L |\mathbf{v}| \frac{\partial C_A}{\partial \mathbf{s}} \tag{14}$$

and

$$J_{A\eta} = -n\alpha_T |\mathbf{v}| \frac{\partial C_A}{\partial n} \tag{15}$$

Let θ be the angle between the local velocity vector and the direction locally perpendicular to the reaction front [Fig. 2(c)]. Then, $J_{A\beta}$ is given by

$$J_{A\beta} = J_{A\eta} \sin \theta + J_{As} \cos \theta$$

$$= -n\alpha_{T} |\mathbf{v}| \frac{\partial C_{A}}{\partial \eta} \sin \theta - n\alpha_{L} |\mathbf{v}| \frac{\partial C_{A}}{\partial s} \cos \theta$$

$$= -n\alpha_{T} |\mathbf{v}| \frac{\partial C_{A}}{\partial \beta} \sin^{2} \theta - n\alpha_{L} |\mathbf{v}| \frac{\partial C_{A}}{\partial \beta} \cos^{2} \theta$$

$$= -n(\alpha_{L} \cos^{2} \theta + \alpha_{T} \sin^{2} \theta) |\mathbf{v}| \frac{\partial C_{A}}{\partial \beta}$$

$$= -n\alpha_{\beta} |\mathbf{v}| \frac{\partial C_{A}}{\partial \beta}$$
(16)

where $\alpha_{\beta} = \alpha_L \cos^2 \theta + \alpha_T \sin^2 \theta$ = dispersivity in the β direction; and D_{β} = dispersion coefficient in the β direction, given by

$$D_{\beta} = \alpha_{\beta} |\mathbf{v}| \tag{17}$$

The final expression in Eq. (16) is obtained by substituting Eqs. (14) and (15) into the first line to obtain the second line, and the third line follows from the second line through the use of the chain rule on the partial derivatives of C_A .

Integrating Eq. (12) over dimensionless time after substituting Eqs. (16) and (17) demonstrates the relationship between the global measure $M_{\rm rxn}(t)$ and the three local mixing measures:

$$M_{\text{rxn}}(t) = b \int_{0}^{t} \oint_{\Gamma} J_{A\beta} d\Gamma dt'$$

$$= nb \int_{0}^{t} \oint_{\Gamma} \frac{\partial C_{A}}{\partial \beta} D_{\beta} d\Gamma dt'$$

$$= nb \int_{0}^{t} \oint_{\Gamma} \frac{\partial C_{A}}{\partial \beta} \alpha_{\beta} |\mathbf{v}| d\Gamma dt'$$
(18)

Last, we considered one local measure of spreading called instantaneous strain, ζ (Zhang et al. 2009), which is given by

$$\zeta = \frac{d\rho}{dt} \frac{\Delta t}{\rho} \approx \frac{\Delta \rho}{\rho} \tag{19}$$

where ρ = length of a small arc of reaction front Γ ; Δt = time interval over which the strain is calculated; and $\Delta \rho$ = change in the arc length over time Δt . In this study, strain was estimated by calculating $\Delta \rho$ over a time interval of $\Delta t = 0.016$. The concentration gradient $\partial C_A/\partial \beta$ was approximated through linear interpolation of $C_A(\beta)$ at each point along the reaction front. We applied a Savitzky-Golay filter (Orfanidis 1995) to the concentration gradient along the reaction front to remove noise resulting from the numerical solution. We used a second order polynomial, with a frame length (normalized by the number of points along the curve) of between 0.0382 and 0.4437 to ensure maximum smoothing while still preserving the spatial character. Then, $M_{\rm rxn}$ was calculated from Eq. (18) using this smoothed curve and is plotted as dots in Fig. 4(a). The results are visually indistinguishable from the those calculated using Eqs. (10) and (11), verifying the accuracy of the smoothed curves.

Results for a Homogeneous Aquifer

Fig. 4(a) shows that $M_{\rm rxn}(t)$ (normalized by M_{Ao}) grows with time for each protocol. Compared to the uniform protocol [no active spreading, Fig. 4(d)], the diverging and dipole protocols produce more reaction, with the dipole protocol producing only slightly more. On the other hand, the converging and stagnation protocols produce less reaction. Therefore, having active spreading is not sufficient to enhance reaction relative to uniform flow.

For each protocol, the temporal evolution of the dispersive mass flow rate of species A across the reaction front, $dM_{\rm rxn}/dt$, is shown in Fig. 4(b) (normalized by M_{Ao}). For the diverging, dipole, and uniform protocols, $dM_{\rm rxn}/dt$ decreases monotonically at a decreasing rate. Both the converging and stagnation protocols, however, show brief periods when $dM_{\rm rxn}/dt$ increases. At early times, $dM_{\rm rxn}/dt$ for the diverging and dipole protocols is higher than for the uniform protocol, and it is lower for later times. The opposite behavior is observed for the converging and stagnation protocols [Fig. 4(e)].

The premise of active spreading is to increase the length L_{Γ} of the reaction front, which, in turn, increases the length along which

mixing and, therefore, reaction can occur. The temporal evolution of L_{Γ} for each protocol is shown in Fig. 4(c) (normalized by the initial length of the reaction front L_{Γ_0}). The position of the reaction front was obtained by finding the zero contour of $C_{A+C}-C_{B+C}$ in Matlab version R2020a, to which we applied a Savitzky-Golay filter (Orfanidis 1995) to remove noise resulting from the numerical solution. We used a second order polynomial with a frame length (normalized by the number of points along the curve) of between 0.0382 and 0.1656 to ensure maximum smoothing while still preserving the spatial character.

With uniform flow, as the plumes move downgradient, the reaction front propagates into the plume of species A from a Lagrangian perspective [Fig. 5(a)], because the concentration of species B is higher than the concentration of species A. Therefore, the length of the reaction front increases over time, even without active spreading. With active spreading, the reaction front length increases even more [Fig. 4(f)]. However, the reaction front length does not by itself explain the relative amount of reaction shown in Fig. 4(a). For example, the stagnation protocol has the longest reaction front [dashed line in Fig. 4(a)], but it produces the least amount of reaction [dashed line in Fig. 4(a)]. Therefore, global stretching alone is not sufficient to explain the global amount of reaction.

To investigate the causes of the relative amount of contaminant degradation across the four active spreading protocols, we evaluate the local measures along the reaction fronts. Figs. 5–9 show the plumes of species A and B and the position of the reaction fronts at four different times for the uniform, diverging, converging, dipole, and stagnation protocols, respectively, along with the time evolution of dispersion coefficient D_{β} , instantaneous strain ζ , concentration gradient $\partial C_A/\partial \beta$, and dispersive mass flux $J_{A\beta}$. Note that the shading for C_A in the plume plot is different from in Fig. 2 to allow for more resolution.

The overall mass reacted depends, in part, on the reaction front length. Comparison of Fig. 4(c) and Figs. 5(b)-9(b) show that reaction front length is correlated with the amount of positive strain. Instantaneous strain is positive where the reaction front is stretched locally. Local stretching occurs where flow is diverging and the reaction front is perpendicular to flow, for example, at ℓ/L_{Γ} = 0 and 0.5 for the diverging and stagnation protocols for all times (Figs. 6 and 9); and at $\ell/L_{\Gamma} = 0$ for dipole protocol at early times (Fig. 8). Local stretching also occurs where flow is converging and the reaction front is parallel to flow, for example, at $\ell/L_{\Gamma}=0.25$ for the converging protocol at all times (Fig. 7); and at $\ell/L_{\Gamma} \approx 0.3$ for the dipole protocol at later times (Fig. 8). These relationships are summarized in Table 2. The stagnation protocol has the longest reaction front, consistent with its having the highest positive strain [Figs. 5(b)-9(b)], followed by the converging, diverging, dipole, and uniform protocols, in decreasing order. For the converging protocol, the amount of positive strain is low at early times and increases at later times [white shaded region in Figs. 7(b and c)], consistent with the reaction front length being shorter at early times and higher at later times relative to the other protocols [Fig. 4(c)]. These results are summarized in Table 3.

The overall mass reacted also depends on the dispersive mass flux. Figs. 5(c)–9(c) show that in all cases the spatial average of the dispersive mass flux $J_{A\beta}$ across the reaction front decreases over time. Because the instantaneous reaction rate is directly related to the dispersive mass flux, the decrease is $J_{A\beta}$ is consistent with the decreasing trend of $dM_{\rm rxn}/dt$ in Fig. 4(b). The differences in the global reaction rate and other global measures across the different protocols can be explained by the variability of D_{β} and $\partial C_A/\partial \beta$, which are components of $J_{A\beta}$, along the front.

Figs. 5(b)–9(b) show the variation of $D_{\beta} = \alpha_{\beta} |\mathbf{v}|$ along the reaction front for all protocols. The value of local dispersivity α_{β}

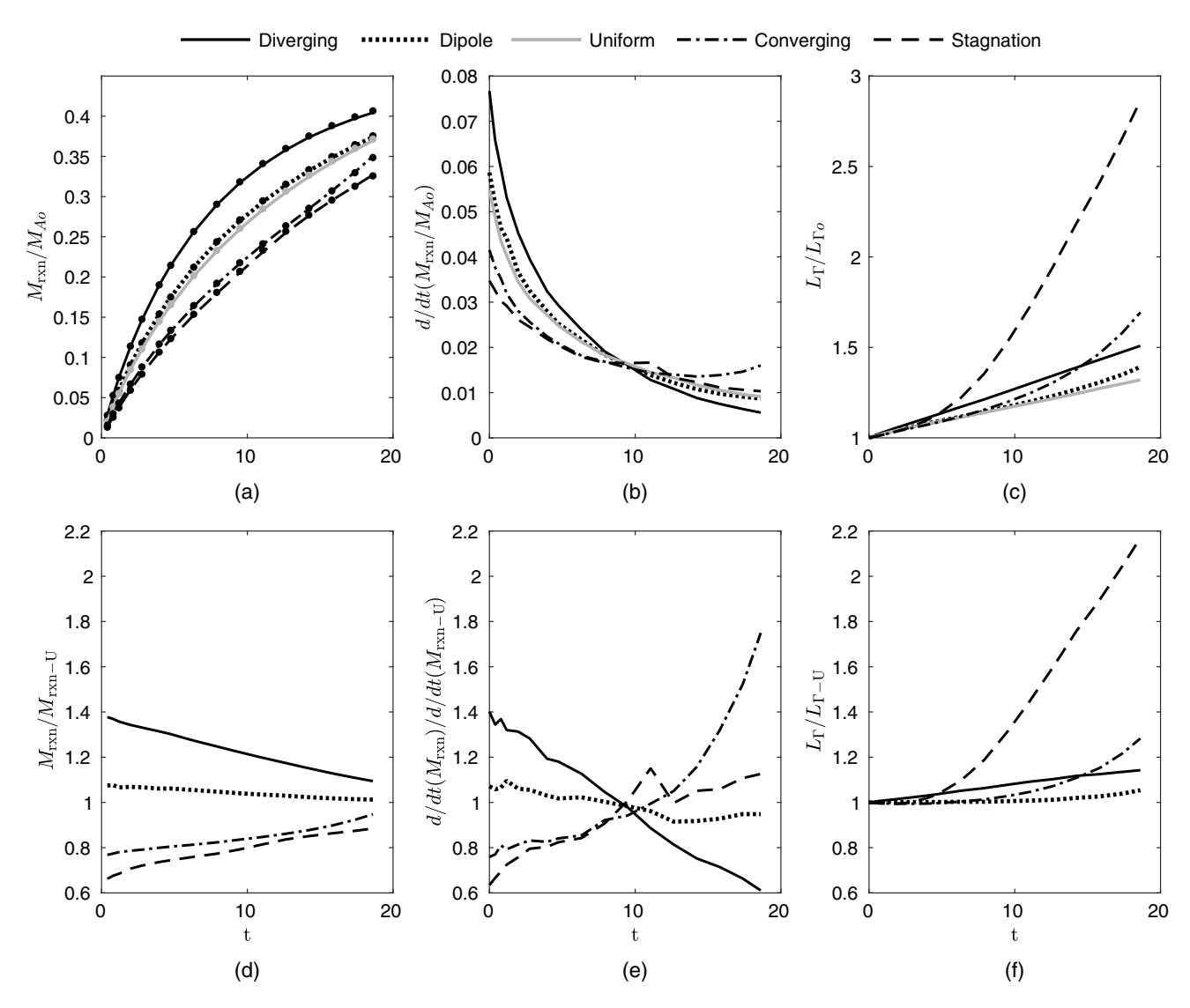


Fig. 4. Temporal evolution of measures of global spreading, mixing, and reaction: (a) temporal evolution of the cumulative mass reacted of species A, $M_{\rm rxn}$, calculated using Eq. (10) (lines) and Eq. (18) (points) and normalized by M_{Ao} ; (b) temporal evolution of the the dispersive mass flow rate of species A across the reaction front, $d/dt(M_{\rm rxn}/M_{Ao})$; (c) temporal evolution of the length of the reaction front L_{Γ} normalized by the initial length $L_{\Gamma o}$; (d) $M_{\rm rxn}$ normalized by $M_{\rm rxn_U}$; (e) $d/dt(M_{\rm rxn})$ normalized by $d/dt(M_{\rm rxn-U})$; and (f) L_{Γ} normalized by $L_{\Gamma-U}$. The subscript U refers to the uniform protocol.

depends on the direction of the local velocity vector relative to the orientation of the reaction front through Eq. (16), as summarized in Table 3. Because $\alpha_L > \alpha_T$, α_β is higher where the reaction front is perpendicular to the local flow. Therefore, D_β tends to be higher where the reaction front is perpendicular to local flow.

The magnitude of velocity also affects D_{β} . All protocols have approximately the same mean velocity but different spatial distributions of velocity, which impacts the amount of reaction. The diverging protocol exhibits high velocities for x < 0 (Fig. 3), which corresponds to the locations of the reaction front at early times, when the concentration gradient remains high [Figs. 5(c)–9(c)]. Therefore, the diverging protocol exhibits high dispersive mass flux and high amounts of reaction, especially at early times [Fig. 4(d)]. However, the converging protocol exhibits high velocities for x > 0 (Fig. 3), which corresponds to locations of the reaction front at later times, when the concentration gradient has diminished [Figs. 5(c)–9(c)]. Therefore, the converging protocol exhibits less dispersive mass flux and less overall reaction, with the rate of reaction increasing over time [Fig. 4(d)]. The dipole protocol exhibits

moderate velocities near the upstream and downstream wells and lower velocities near x=0, resulting in less reaction than the diverging protocol at early times [Fig. 4(d)], but the rate of reaction decreases more slowly [Fig. 4(e)]. The stagnation protocol also exhibits moderate velocities at the upstream and downstream wells, but it has very low velocities near the stagnation point, so D_{β} is low near the stagnation point even though the reaction front is perpendicular to local flow, leading to less reaction overall than the other protocols.

The concentration gradient, $\partial C_A/\partial \beta$ [Figs. 5(c)–9(c)], is smoothed by dispersion and negative strain and is sharpened by positive strain. For a given protocol, the concentration gradient decreases more quickly over time where D_β is high and more slowly where it is low. For example, in all protocols except the stagnation protocol, $\partial C_A/\partial \beta$ decreases rapidly near $\ell/L_\Gamma=0$ and 0.5 and slowly near $\ell/L_\Gamma=0.25$, corresponding to high and low values, respectively, of D_β . The concentration gradient decreases most rapidly where strain is negative and the reaction front is perpendicular to flow (i.e., $\alpha_\beta \approx \alpha_L$, so D_β is high), such as near $\ell/L_\Gamma=0$ or 0.5

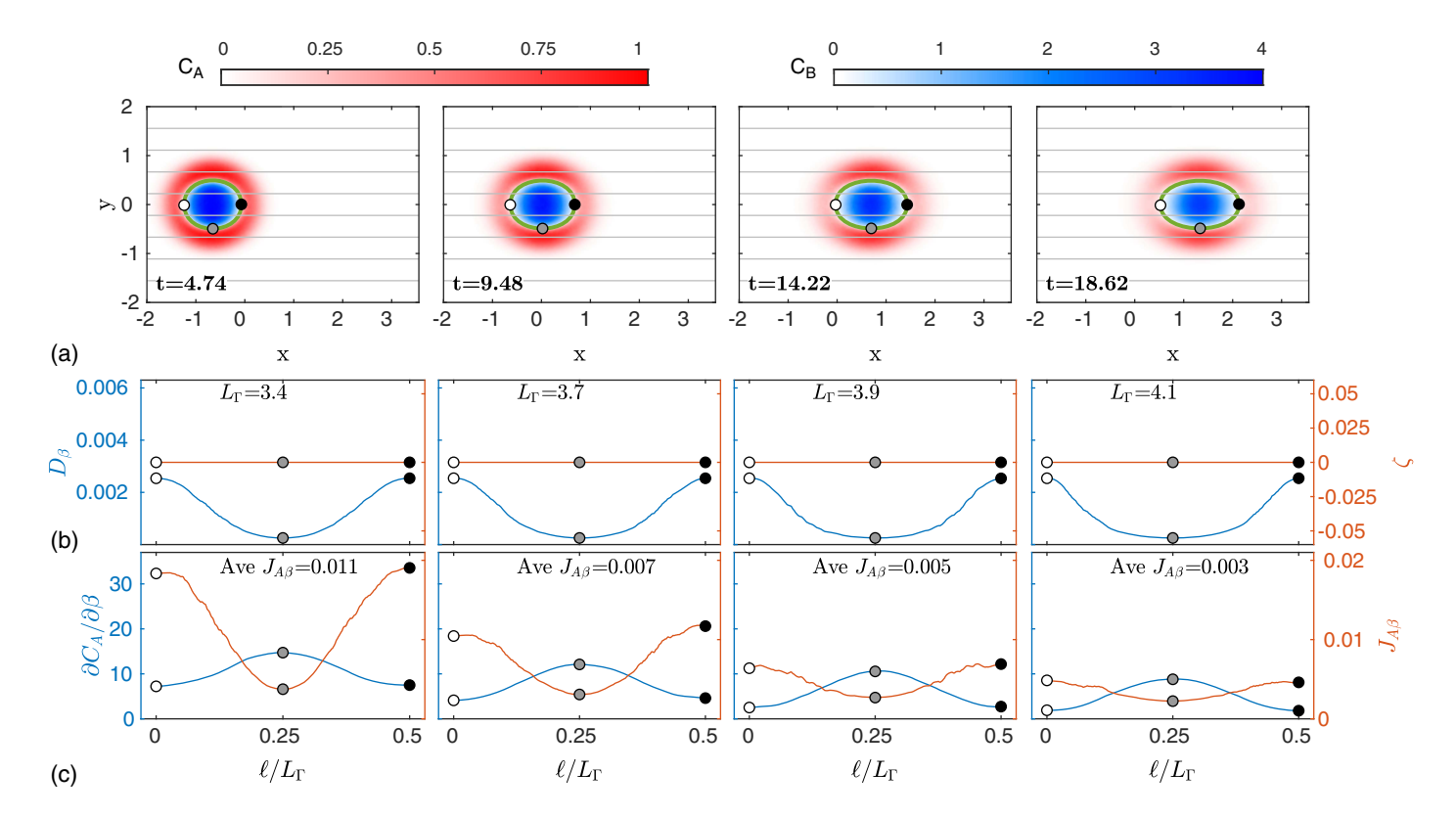


Fig. 5. Local analysis of results of uniform protocol at four times: (a) plumes of species A (outer plume) and B (inner plume), reaction front (between A and B line), and streamlines (gray lines); and (b and c) local measures versus normalized distance ℓ/L_{Γ} along the reaction front, with $\ell/L_{\Gamma}=0$ shown by the white circle.

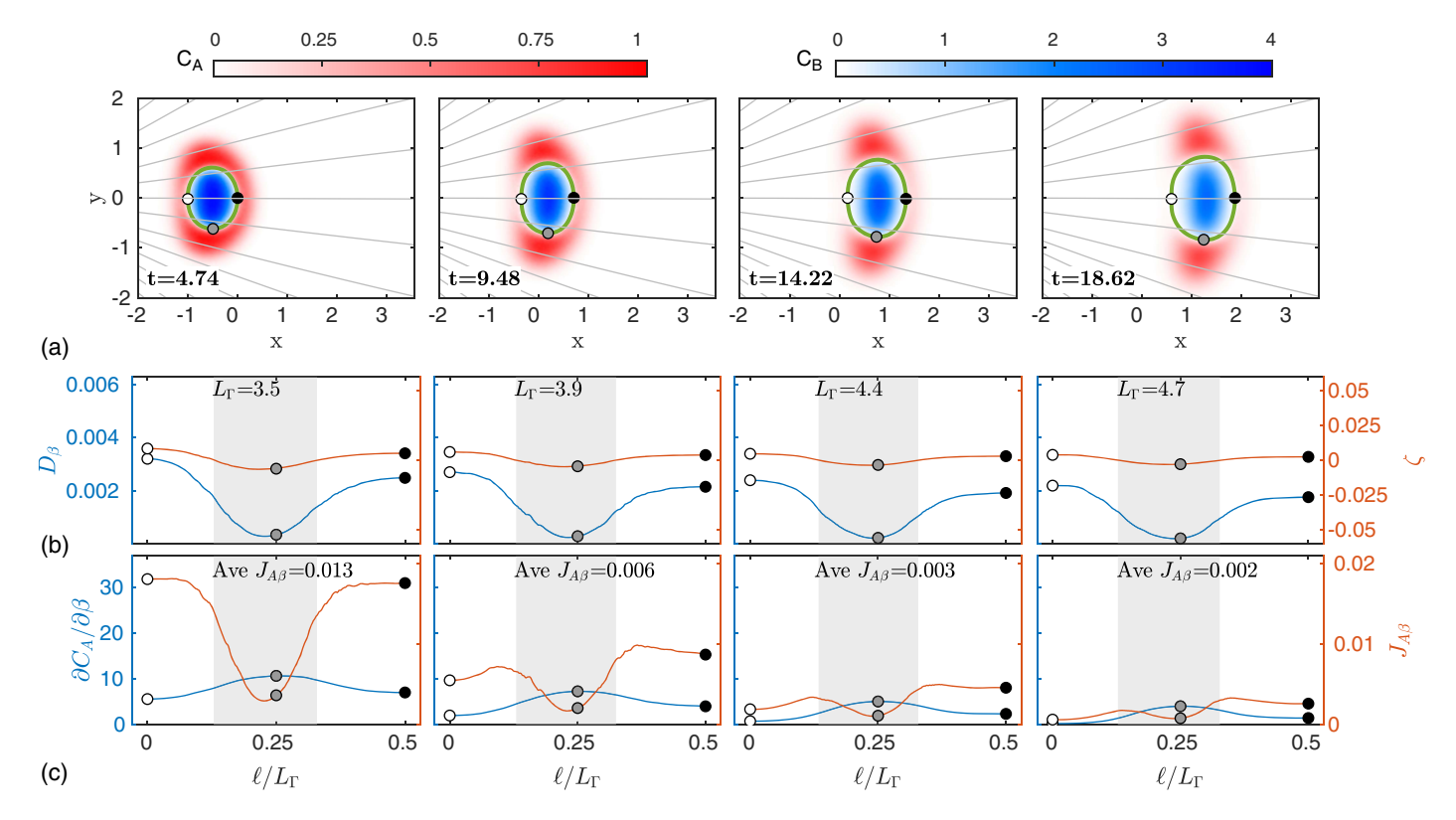


Fig. 6. Local analysis of the diverging protocol at four different times: (a) plumes of species A (red) and B (blue), reaction front (green line), and streamlines (gray lines); and (b and c) local measures versus normalized distance ℓ/L_{Γ} along the reaction front, with $\ell/L_{\Gamma}=0$ shown by the white circle. Gray shading indicates negative strain.

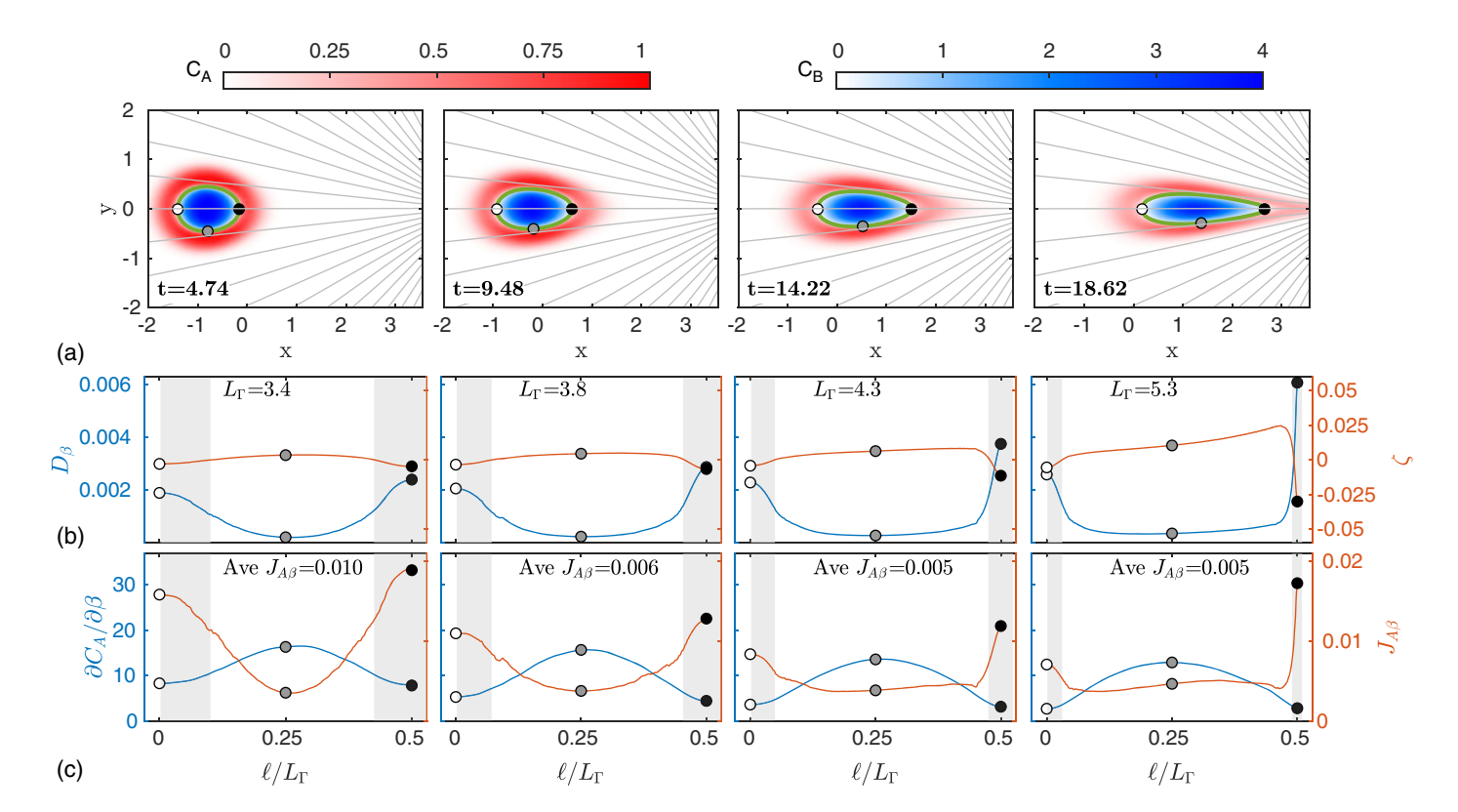


Fig. 7. Local analysis of results of converging protocol at four times: (a) plumes of species A (red) and B (blue), reaction front (green line), and streamlines (gray lines); and (b and c) local measures versus normalized distance ℓ/L_{Γ} along the reaction front, with $\ell/L_{\Gamma}=0$ shown by the white circle. Gray shading indicates negative strain.

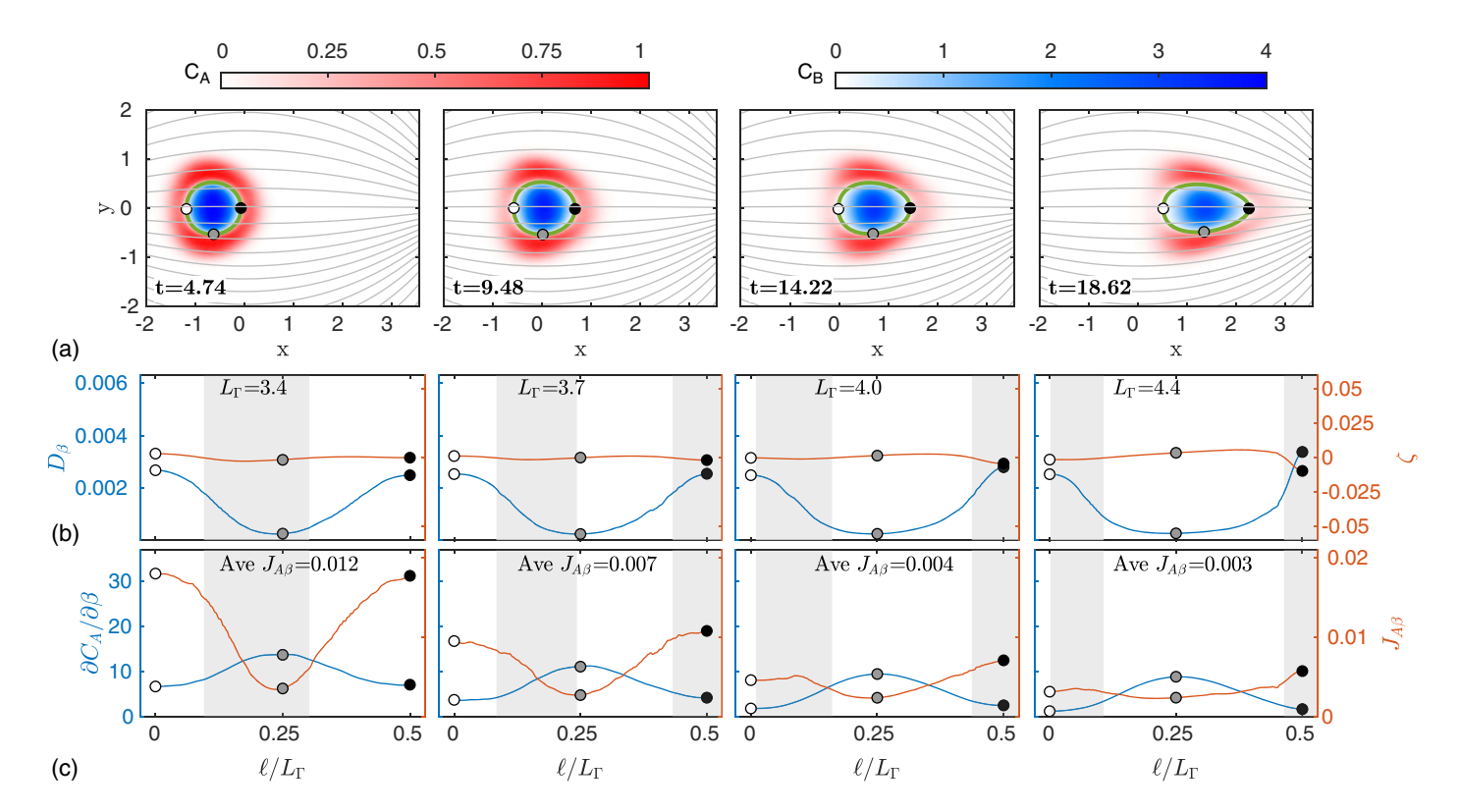


Fig. 8. Local analysis of the dipole protocol at four different times: (a) plumes of species A (red) and B (blue), reaction front (green line), and streamlines (gray lines); and (b and c) local measures versus normalized distance ℓ/L_{Γ} along the reaction front, with $\ell/L_{\Gamma}=0$ shown by the white circle. Gray shading indicates negative strain.

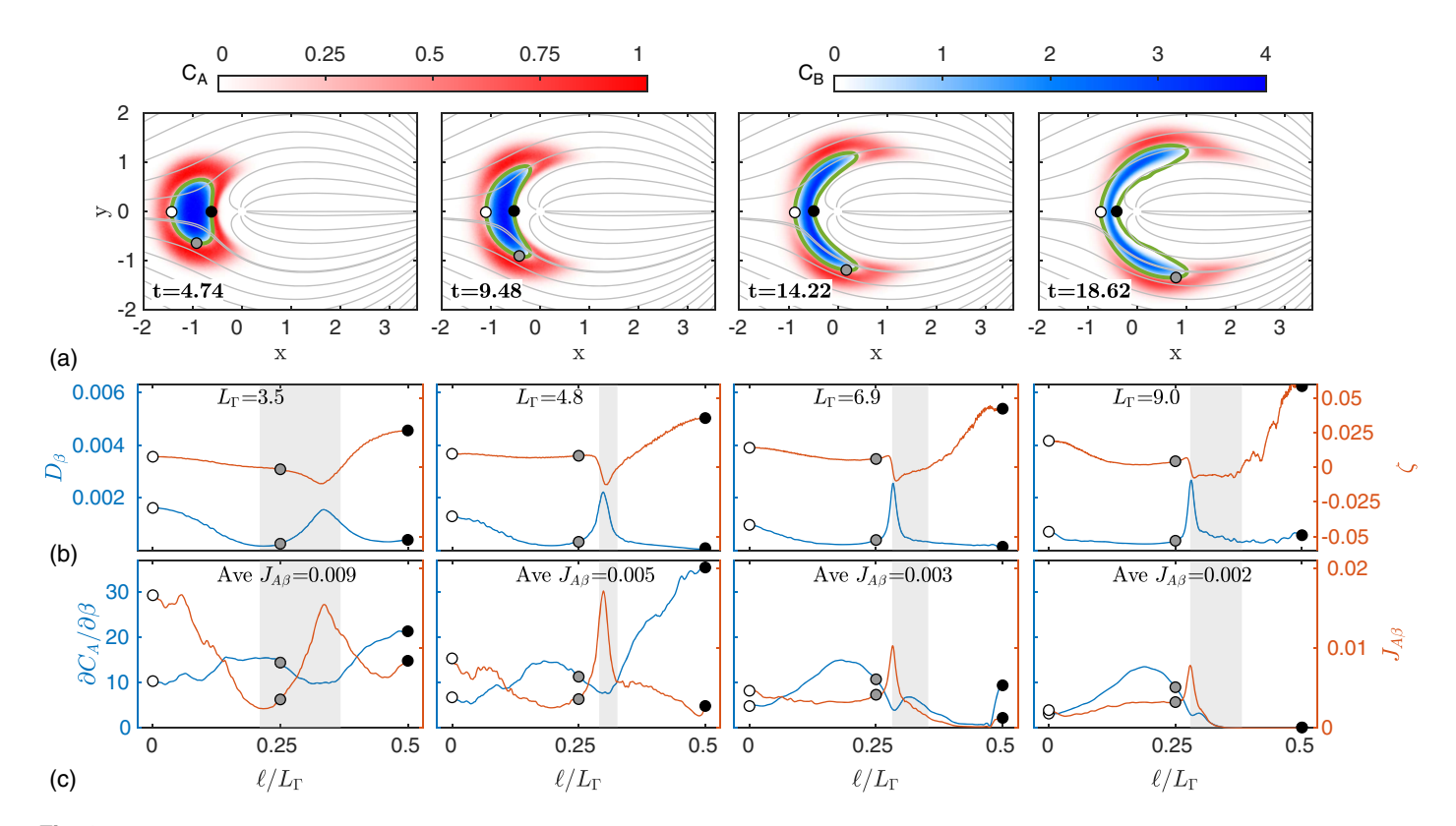


Fig. 9. Local analysis of the stagnation protocol at four different times: (a) plumes of species A (red) and B (blue), reaction front (green line), and streamlines (gray lines); and (b and c) local measures versus normalized distance ℓ/L_{Γ} along the reaction front, with $\ell/L_{\Gamma}=0$ shown by the white circle. Gray shading indicates negative strain.

Table 3. Summary of the relationship between the reaction front and flow conditions on stretching and mixing parameters

Character	Orientation of reaction front		
of flow	⊥ to flow	to flow	
Diverging	$\zeta > 0$	ζ < 0	
	$\alpha_{eta}pprox lpha_{L}$	$\alpha_{\beta} pprox \alpha_{T}$	
	$\begin{array}{c} \zeta > 0 \\ \alpha_{\beta} \approx \alpha_{L} \\ \frac{\partial C_{A}}{\partial \beta} \ \text{decreases moderately} \end{array}$	$ \zeta < 0 \\ \alpha_{\beta} \approx \alpha_{T} \\ \frac{\partial C_{A}}{\partial \beta} \text{ decreases moderately} $	
Converging	$\zeta < 0$	$\zeta > 0$	
	$\alpha_{eta}pprox lpha_{L}$	$\alpha_{\beta} pprox \alpha_{T}$	
	$\zeta < 0$ $\alpha_{eta} pprox \alpha_{L}$ $rac{\partial C_{A}}{\partial eta}$ decreases rapidly	$\begin{aligned} &\zeta>0\\ &\alpha_{\beta}\approx\alpha_{T}\\ &\frac{\partial C_{A}}{\partial\beta} \text{ decreases slowly} \end{aligned}$	

in the converging protocol. However, $\partial C_A/\partial \beta$ decreases most slowly where strain is positive and the reaction front is parallel to flow (i.e., $\alpha_{\beta} \approx \alpha_T$, so D_{β} is low), such as near $\ell/L_{\Gamma}=0.25$ in the converging protocol. The concentration gradient decreases at a moderate rate where $\zeta>0$ and D_{β} is high and where $\zeta<0$ and D_{β} is low. These behaviors are summarized in Table 3. In uniform flow, $\zeta=0$ everywhere at all times, which neither sharpens nor smooths the concentration gradient. Therefore, in the uniform protocol, $\partial C_A/\partial \beta$ decreases over time as a result of dispersion only. As a result, the rate of degradation in the converging protocol increases over time relative to the uniform protocol because the concentration gradient remains high (due to positive strain along most of the reaction front; see Table 3). However, the rate of degradation in the diverging protocol decreases over time relative to the uniform protocol, because the concentration gradient decreases

more rapidly (high α_{β} where strain is positive, and low α_{β} where strain is negative).

Given that the dispersive mass flux $J_{A\beta}$ [Eq. (16)] depends on the product of D_{β} and $\partial C_A/\partial \beta$, and $\partial C_A/\partial \beta$ also depends on D_{β} , $J_{A\beta}$ is more sensitive to the spatiotemporal pattern of D_{β} than to that of $\partial C_A/\partial \beta$. Therefore, $J_{A\beta}$ [Figs. 5(c)–9(c)] follows the same pattern as D_{β} except where the concentration of species A (and therefore its concentration gradient and mass flux) falls to zero (e.g., near $\ell/L_{\Gamma} = 0$ and 0.5 at later times in the diverging protocol, when $C_A \approx 0$ but D_β is relatively high). Therefore, the overall amount of reaction is higher in active spreading protocols in which the reaction front tends to be more perpendicular to the local velocity vectors, that is, where $\alpha_{\beta} \approx \alpha_{L}$, such as in the diverging and dipole protocols. Likewise, the overall amount of reaction is lower in active spreading protocols in which the reaction front tends to be more parallel to the local velocity vectors, such as in the converging and stagnation protocols. For comparison, in uniform flow, the reaction front has equal proportions perpendicular to and parallel to the local velocity vectors, so the amount of reaction in the uniform protocol falls in the middle of the five protocols considered in this work.

Results for Heterogeneous Aquifers

In this section, we investigate how heterogeneity (passive spreading) impacts reaction during active spreading. Reactive transport was simulated in flow fields generated from the four active spreading protocols with nine different heterogeneous hydraulic conductivity (K) fields. Random fields of $\ln K$ were generated using sequential Gaussian simulation (Deutsch and Journel 1992) with a spherical variogram with correlation lengths λ of $\lambda=0.125d$,

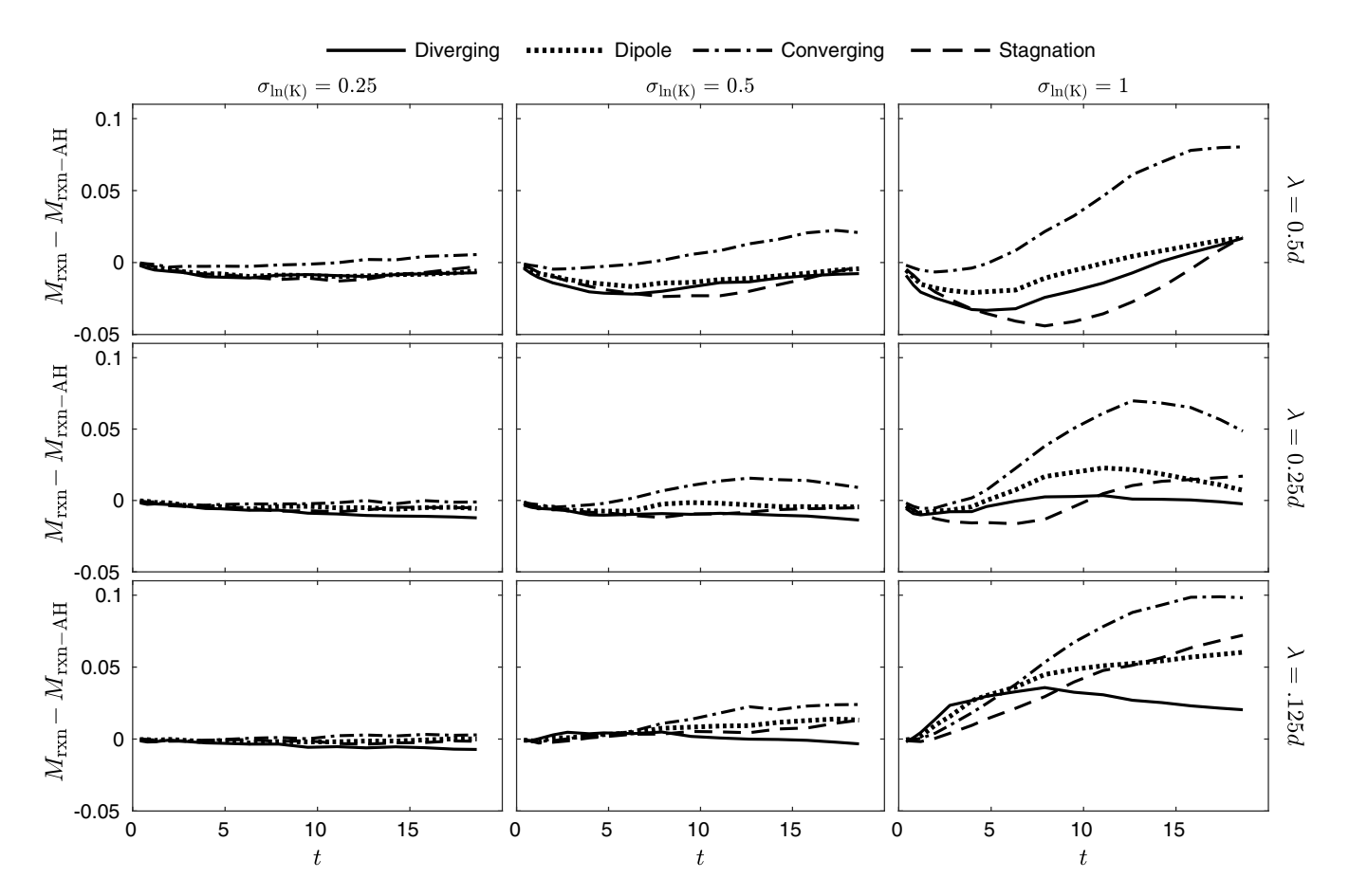


Fig. 10. Plots of $M_{\text{rxn}} - M_{\text{rxn-AH}}$ for the four active spreading protocols in nine different models of heterogeneous aquifers, where $M_{\text{rxn-AH}}$ is M_{rxn} for the respective protocol in the homogeneous aquifer.

0.25d, and 0.5d, with a mean value of dimensionless K of 3.57 and values of $\sigma_{\ln K}$ of 0.25, 0.5, and 1. Plots of the $\ln K$ fields in the vicinity of the wells are shown in Fig. S2. For all simulations presented in this section, species A and B were represented as collections of 6×10^5 and 2×10^5 randomly placed particles, respectively, which had dimensionless masses of 6.53×10^{-7} and 2.73×10^{-6} , respectively. A smaller number of particles were required compared to the simulations in the previous section because only global behavior was analyzed here.

Fig. 10 shows the difference of cumulative mass reacted in the heterogeneous aquifer (active and passive spreading) and the cumulative mass reacted in the homogeneous aquifer, denoted as $M_{\rm rxn-AH}$, (active spreading only) for each protocol and each heterogeneity model. This difference represents the contribution of passive spreading to reaction. For low $\sigma_{\ln K}$, passive spreading contributes little extra reaction for all protocols, and the relative contribution increases as $\sigma_{\ln K}$ increases, with the converging protocol having the largest contribution. At certain times, passive spreading leads to a reduction in the overall amount of reaction, particularly when the combination of the active spreading protocol and the heterogeneity pattern cause the plume to constrict (see Figs. S2–S11 for plots of the plume evolution). The behavior depends on the spatial distribution of $\ln K$, which is consistent with the findings of de Barros et al. (2012).

Fig. 11 shows the ratio of cumulative mass reacted by each active spreading protocol in the heterogeneous aquifer (active and passive spreading) relative to the cumulative mass reacted by the uniform protocol in the heterogeneous aquifer, denoted as $M_{\rm rxn-UHet}$ (passive spreading only). This ratio represents the contribution of

active spreading. The results show that as heterogeneity increases, the contribution of active spreading to reaction also increases, demonstrating that the amount of reaction is strongly controlled by the active spreading protocol, even in heterogeneous aquifers. The results also show that the relative amounts of reaction across the four active spreading protocols remain the same as in homogeneous aquifers, that is, the diverging protocol exhibits the most reaction, followed, in decreasing order, by the dipole, converging, and stagnation protocols. One exception is that as heterogeneity increases, the converging protocol produces more reaction than the other protocols at later times. As heterogeneity increases, the reaction front becomes more irregular, resulting in portions of the reaction front that are more perpendicular to the flow direction near the extraction well, where velocities are high. For example, the third and fourth panels of Fig. S8(c) show that the reaction front near the leading edge of the plume of species B (white shaded region between the blue and red shading) crosses the streamlines (i.e., is perpendicular to the local velocity), while for the homogeneous aquifer [Fig. 7(a)] the reaction front remains aligned with the streamlines. Therefore, the combination of high dispersivity ($\alpha_{\beta} \approx \alpha_{L}$, because portions of the reaction front are perpendicular to flow), high velocity (i.e., high D_{β}), and positive strain enhances reaction. This enhancement also occurs in the dipole protocol, but to a lesser extent.

Discussion

Spreading, mixing, and reaction in porous media are manifestations of spatial or spatiotemporal variations in the velocity field. Spreading, by definition, is the reconfiguration of a plume due to velocity

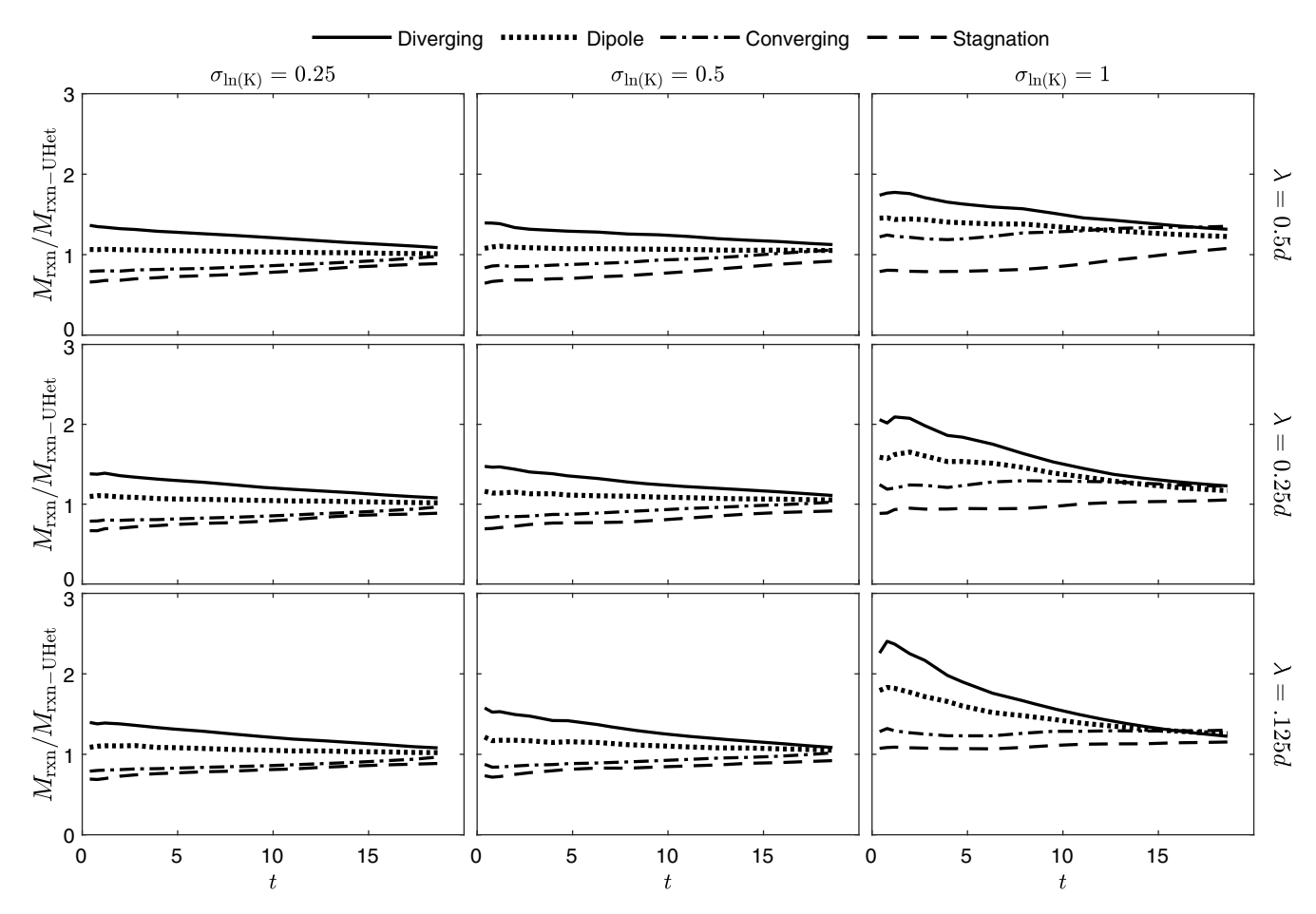


Fig. 11. Plots of $M_{\text{rxn}}/M_{\text{rxn-UHet}}$ for the four active spreading protocols in nine different models of heterogeneous aquifers, where $M_{\text{rxn-UHet}}$ is M_{rxn} for the uniform protocol in each heterogeneous aquifer.

variation; while mixing and reaction tend to be enhanced as a result of spreading. A high degree of spreading has been accomplished under conditions of chaotic advection (Lester et al. 2013; Aref et al. 2017; Speetjens et al. 2021), but spreading can also be accomplished to a lesser degree through natural heterogeneity of the porous medium (passive spreading) and imposed pumping schemes (active spreading).

A number of recent studies have pointed to the intriguing result that stretching may be sufficient to predict reactive transport. Specifically, de Barros et al. (2012) used the Okubo-Weiss parameter to predict reaction based on stretching; Engdahl et al. (2014) found a similar result, that stretching predicts reaction. Both studies argued that reaction depends on flow, which is supported by the results of the present study. However, both studies assumed a constant isotropic dispersion coefficient and, therefore, did not account for the impact of the orientation of the reaction front within the flow field or on the spatial variation of velocity. In the present study, we used a dispersion coefficient that varied with flow direction and magnitude of velocity, which is the observed behavior of solute transport at the plume scale. We quantified stretching as the length of the reaction front, and we showed (Fig. 4) that stretching alone is not sufficient to enhance reaction—the stagnation protocol exhibits double the amount of stretching of any other method, yet it produces the least amount of reaction. In fact, the results showed that spatial variations in velocity (i.e., the required ingredient for spreading) do not necessarily enhance reaction. Relative to uniform flow, two of the four protocols we investigated (converging and stagnation) produce less reaction than uniform flow [Fig. 4(d)], so in those cases, active spreading inhibited reaction. The key conclusion here is that global measures are not sufficient to predict the overall amount of contaminant degradation.

Our analysis of local relationships between velocity field and plume geometry allowed us to identify that instantaneous reactions in porous media proceed more quickly where the plume interface, and therefore the reaction front, is perpendicular to local velocity, due to the notion that longitudinal dispersivity is greater than transverse dispersivity. These results are consistent with and expand upon previous works that considered simpler plume geometries.

In the context of flow and transport in porous media, those studying lamellae (Meunier and Villermaux 2010; Le Borgne et al. 2013; de Anna et al. 2014) have articulated the interplay between stretching forming longer lamellae versus diffusion coalescing lamellae together. A similar interplay has been explored by researchers studying spreading and mixing using the scalar dissipation rate that, under certain assumptions described by de Dreuzy et al. (2012), is (1/2)dM/dt, where M is the integral over space of the concentration squared (Le Borgne et al. 2010; de Dreuzy et al. 2012; Engdahl et al. 2013). As a group, these papers explain the interplay between spreading that sharpens gradients and elongates interfaces versus mixing that softens gradients and blurs interfaces. While these previous works often considered simpler plume geometries, the results of the present study were consistent with their findings. For example, studies that considered one species invading another species (Le Borgne et al. 2013; Perez et al. 2020) identified the formation of lamella within a pore that sharpened concentration gradients and promoted mixing and reaction. At the plume scale, which was the focus of the present study, the plumes form lamella-like features as they travel through heterogeneous material (see Figs. S3–S11), which locally sharpens concentration gradients. Consistent with studies of lamella formation at the pore scale, we found that increasing heterogeneity leads to high amounts of reaction (Figs. 10 and 11).

As another example, our results were consistent with results of studies that considered a plume emanating from a continuous source, in which the plume boundary is aligned with the flow direction and mixing across the boundary is controlled by transverse dispersion. Cirpka et al. (2011) found that small-scale heterogeneity enhanced the mixing and reaction of such a plume. This result is consistent with our finding that heterogeneity increased the amount of reaction in the converging protocol relative to the uniform protocol. Without heterogeneity (Fig. 7), the reaction front

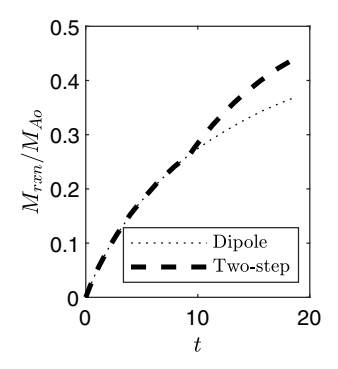


Fig. 12. Temporal evolution of cumulative mass reacted of species A, M_{rxn} , normalized by M_{Ao} for the dipole and two-step dipole protocols.

is aligned with the flow direction throughout most of its extent, especially where velocity is high (near the extraction well), but with heterogeneity, portions of the reaction front are perpendicular to the local flow direction and longitudinal dispersion dominates, enhancing reaction. In another study with a plume emanating from a continuous source, Rolle et al. (2009) found that temporal variation in uniform flow had essentially no effect on reaction. This behavior is consistent with the results of our study; that is, the plume boundary remained aligned with the flow direction, even as the velocity changed, but reaction proceeded most rapidly where the reaction front was perpendicular to the local velocity, so the temporal change in uniform flow had little effect.

To further demonstrate that a reaction front aligned perpendicular to the local flow field enhances reaction, we repeated the dipole protocol; however, after t = 9.48, we rotated the dipole by 90° so that injection occurred at (0, +4.44) and extraction occurs at (0, -4.44). Fig. 12 shows that cumulative mass reacted increases when the dipole orientation is changed, leading to more cumulative mass reacted for the two-step dipole protocol as compared with the standard one-step dipole protocol. The cause of this behavior is apparent through comparison of Figs. 8 and 13, which show the plume evolution and local measures along the reaction front at various times for the one-step dipole and two-step dipole protocols, respectively. Note that the limits on the plume plot and on the plot of dispersive mass flux are different in the two figures. In both figures, the left-hand panels show results for t = 4.74, and the figures are identical because both protocols had the same flow rate. The second time that is plotted for the two-step dipole protocol (Fig. 13) is just after the change in the flow field, very close in time to the second time plotted in Fig. 8. At this time, the highest concentration gradients along the reaction front occur near $\ell = 0.25 L_{\Gamma}$. In the one-step dipole protocol, D_{β} is low at that

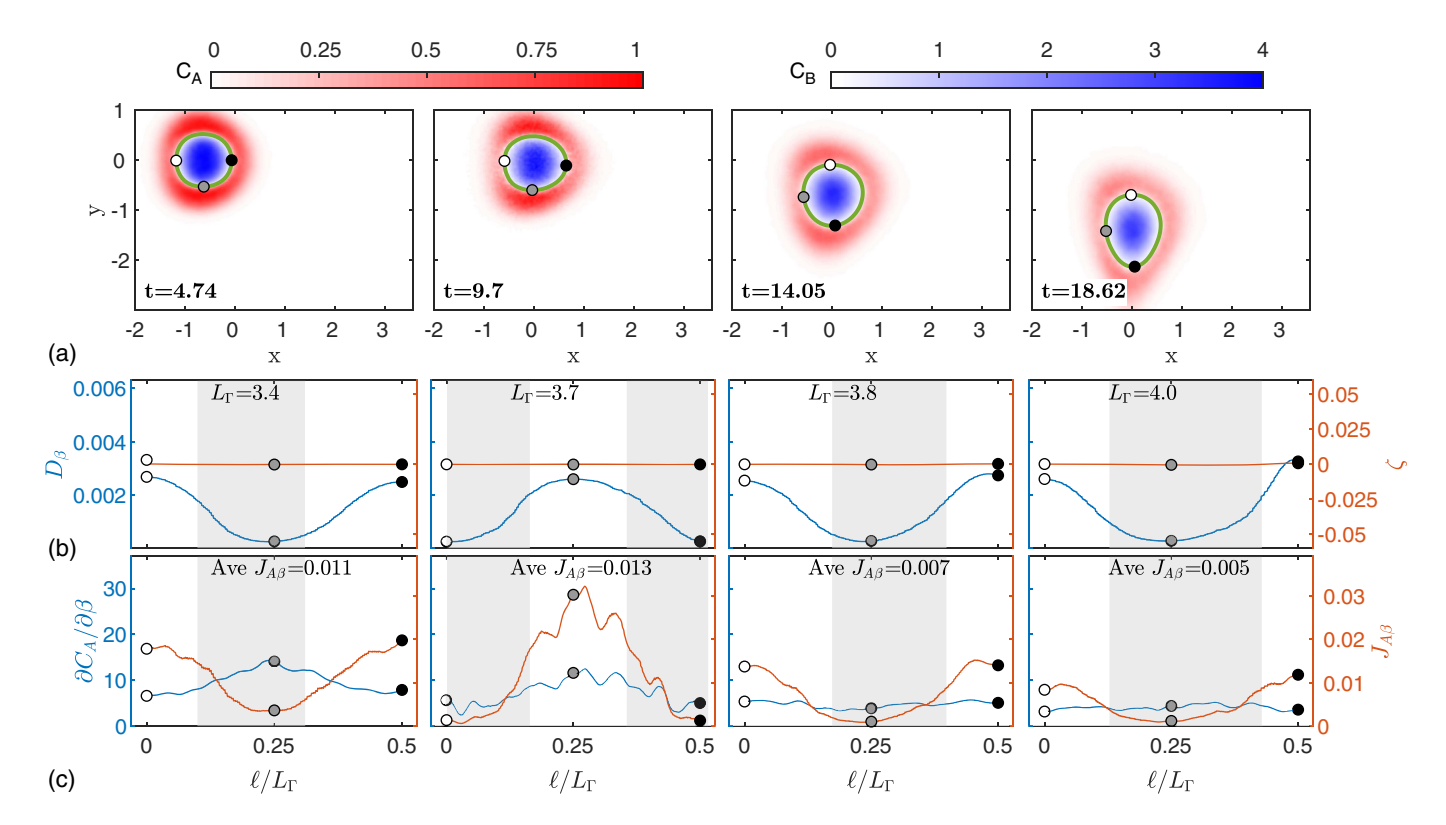


Fig. 13. Local analysis of the two-step dipole protocol at four different times: (a) plumes of species A (red) and B (blue), reaction front (green line), and streamlines (gray lines); and (b and c) local measures versus normalized distance ℓ/L_{Γ} along the reaction front, with $\ell/L_{\Gamma}=0$ shown by the white circle. Gray shading indicates negative strain.

point because the reaction front is aligned with the local flow direction. However, in the two-step dipole protocol, the flow field is rotated 90°, so the reaction front is perpendicular to the flow direction at that point, leading to high D_{β} , high $J_{A\beta}$, and, therefore, a higher reaction rate. Over time, the concentration gradients are smoothed as the reaction front propagates toward the operating extraction well [at (x,y)=(0,-4.44)], leading to lowering of $J_{A\beta}$ and the reaction rate.

At the pore scale, smoothing of concentration gradients is driven by molecular diffusion; therefore, the Peclet number, which reflects the relative contributions of advection and molecular diffusion, is a fundamental parameter. At the plume scale, smoothing of the concentration gradients occurs through molecular diffusion, but at this larger scale it is also driven by velocity variations that bring together water parcels that take different paths around solid grains and around small-scale low permeability features. In groundwater remediation applications, the Peclet number is typically large, particularly near the active spreading wells, so much of the reaction is driven by advection. A sensitivity analysis was conducted on the molecular diffusion coefficient in our simulations and showed that the amount of reaction is not sensitive to molecular diffusion (see Fig. S1).

An important caveat is that the simulations presented here, like many others in the reactive transport literature, assume instantaneous bimolecular reaction of $A+B\to C$, where all species are aqueous and nonsorbing. Not all of these assumptions will hold in practical situations; for example, it is known that pumping schemes that optimize degradation of sorbing contaminants are quite different from those that optimize degradation of nonsorbing contaminants (Neupauer and Mays 2015). Future work will be required to generalize the results of this study beyond the simplified chemistry assumed here. The goal of this study was to demonstrate that it may be possible to improve practical applications of reactive transport in porous media by taking into account the geometry of plume spreading.

Conclusion

Several recent studies have shown that velocity variations within a pore (Meunier and Villermaux 2010; Le Borgne et al. 2013) or in a porous medium at larger scales (de Barros et al. 2012; Engdahl et al. 2014) lead to elongation of fluid interfaces and sharpening of concentration gradients at the interface, both of which can enhance mixing and, therefore, reaction. In this work, we found that elongation of the interface and sharpening of the gradients was not sufficient to enhance reaction. Furthermore, some patterns of spatially varying velocity actually inhibited reaction. In other words, a global enhancement of reaction is not necessarily the result of global stretching of a plume interface but rather is a result of local characteristics of flow and plume geometry along the reaction front. Therefore, the objective of the present study was to identify the local mechanisms that lead to a global enhancement of reaction.

In this study, we evaluated the spreading, mixing, and reaction of two contiguous solute plumes in porous media under uniform flow conditions and under four different active spreading protocols: diverging, converging, dipole, and stagnation (Fig. 3). We considered irreversible, instantaneous bimolecular reaction, in which reaction takes place along a narrow moving reaction front between the two plumes. We demonstrated that the amount of reacted mass is equivalent to the cumulative mass of the species that disperses across the reaction front.

Reaction occurs because the two reactant species come together by dispersion across the reaction front. By definition, the local dispersive mass flux across the reaction front depends on the local concentration gradient and the local dispersion coefficient, both defined in the direction perpendicular to the reaction front. To discern the contributions of each of these to reaction, we evaluated the temporal evolution of characteristics of the local flow field and plume along the moving reaction front. We found that the spatial variability in the flow field and the position of the reaction front within it controls the amount of reaction according to the orientation of the reaction front relative to the local velocity and whether flow is diverging or converging. The highest amount of reaction occurs when flow is diverging and the reaction front is perpendicular to the local velocity. In these locations, dispersion is dominated by longitudinal dispersivity, which is greater than transverse dispersivity. In addition, strain is positive, which sharpens the concentration gradient; therefore, although dispersion smooths the concentration gradient, the positive strain partially counteracts the effects of smoothing. The least amount of reaction occurs when the reaction front is aligned parallel to the local velocity, especially where flow is not converging. In these locations, transverse dispersion dominates and negative strain rapidly reduces the concentration gradient.

The active spreading protocols in this study were representative of components of in situ groundwater remediation systems in which an amendment is emplaced in the contaminant plume to react with and degrade the contaminant. These protocols can be used individually or superimposed in space and time to create more robust flow fields that can be designed to address the specific plume geometry, aquifer characteristics, and remediation goals at a particular site. The combination of the protocols in space and time can lead to faster and more complete degradation of the contaminant, as shown with the two-step dipole protocol, which is a superposition in space and time of the diverging and converging protocols.

The flow fields, aquifer heterogeneity models, and reaction chemistry model considered in this study were not exhaustive, and additional complexities may be encountered in practice that have not been addressed here. For example, contaminants may be trapped in low permeability materials which cannot be accessed by the active spreading protocols described here; or contaminants may sorb and desorb kinetically onto the porous material, so the reaction front may not be a discrete linear feature as it was in this study. Nevertheless, the main results of this study are still applicable, that is, the global amount of reaction is controlled by the local mechanisms that bring species together to react, which, in our scenario, were the concentration gradient and dispersion coefficient in the direction locally transverse to the reaction front. Additional work is needed to identify active spreading protocols that can address these more challenging problems.

Data Availability Statement

All data, models, and code generated or used during the study appear or are cited herein.

Acknowledgments

The authors gratefully acknowledge review suggestions from the editor and anonymous referees whose feedback rendered significant advancement to this work. Funding was provided by the National Science Foundation under Grant Nos. EAR-1417005 and EAR-1417017.

Supplemental Materials

Figs. S1–S11 and Eqs. (S1)–(S4) are available online in the ASCE Library (www.ascelibrary.org).

References

- Aref, H., et al. 2017. "Frontiers of chaotic advection." *Rev. Mod. Phys.* 89 (2): 025007. https://doi.org/10.1103/RevModPhys.89.025007.
- Bandopadhyay, A., T. Le Borgne, Y. Méheust, and M. Dentz. 2017. "Enhanced reaction kinetics and reactive mixing scale dynamics in mixing fronts under shear flow for arbitrary Damköhler numbers." Adv. Water Resour. 100 (Feb): 78–95. https://doi.org/10.1016/j.advwatres.2016.12.008.
- Bellin, A., G. Severino, and A. Fiori. 2011. "On the local concentration probability density function of solutes reacting upon mixing." Water Resour. Res. 47 (1): W01514. https://doi.org/10.1029/2010WR009696.
- Berkowitz, B., A. Cortis, M. Dentz, and H. Scher. 2006. "Modeling non-Fickian transport in geological formations as a continuous time random walk." *Rev. Geophys.* 44 (2): RG2003. https://doi.org/10.1029 /2005RG000178.
- Chiogna, G., O. A. Cirpka, P. Grathwohl, and M. Rolle. 2011. "Relevance of local compound-specific transverse dispersion for conservative and reactive mixing in heterogeneous porous media." *Water Resour. Res.* 47 (7): 11. https://doi.org/10.1029/2010WR010270.
- Chiogna, G., D. L. Hochstetler, A. Bellin, P. K. Kitanidis, and M. Rolle. 2012. "Mixing, entropy and reactive solute transport." *Geophys. Res. Lett.* 39 (20): L20405. https://doi.org/10.1029/2012GL053295.
- Cho, M., F. Solano, N. Thomson, M. Trefry, D. Lester, and G. Metcalfe. 2019. "Field trials of chaotic advection to enhance reagent delivery." Ground Water Monit. Rem. 39 (3): 23–39. https://doi.org/10.1111/gwmr.12339.
- Cirpka, O. A., F. P. J. de Barros, G. Chiogna, M. Rolle, and W. Nowak. 2011. "Stochastic flux-related analysis of transverse mixing in twodimensional heterogeneous porous media." Water Resour. Res. 47 (6): 45. https://doi.org/10.1029/2010WR010279.
- de Anna, P., M. Dentz, A. Tartakovsky, and T. Le Borgne. 2014. "The filamentary structure of mixing fronts and its control on reaction kinetics in porous media flows." *Geophys. Res. Lett.* 41 (13): 4586–4593. https://doi.org/10.1002/2014GL060068.
- de Barros, F. P., M. Dentz, J. Koch, and W. Nowak. 2012. "Flow topology and scalar mixing in spatially heterogeneous flow fields." *Geophys. Res. Lett.* 39 (8): L08404. https://doi.org/10.1029/2012GL051302.
- de Dreuzy, J.-R., J. Carrera, M. Dentz, and T. Le Borgne. 2012. "Time evolution of mixing in heterogeneous porous media." Water Resour. Res. 48 (6): W06511. https://doi.org/10.1029/2011WR011360.
- Deutsch, D., and A. Journel. 1992. GSLIB: Geostatistical software library and user's guide. New York: Oxford University Press.
- Engdahl, N. B., D. A. Benson, and D. Bolster. 2014. "Predicting the enhancement of mixing-driven reactions in nonuniform flows using measures of flow topology." *Phys. Rev. E* 90 (5): 051001. https://doi. org/10.1103/PhysRevE.90.051001.
- Engdahl, N. B., T. R. Ginn, and G. E. Fogg. 2013. "Scalar dissipation rates in non-conservative transport systems." *J. Contam. Hydrol.* 149 (Jun): 46–60. https://doi.org/10.1016/j.jconhyd.2013.03.003.
- Gramling, C. M., C. F. Harvey, and L. C. Meigs. 2002. "Reactive transport in porous media: A comparison of model prediction with laboratory visualization." *Environ. Sci. Technol.* 36 (11): 2508–2514. https://doi. org/10.1021/es0157144.
- Harbaugh, A. W., C. D. Langevin, J. D. Hughes, R. N. Niswonger, and L. F. Konikow. 2017. MODFLOW-2005 version 1.12.00, the U.S. Geological Survey modular groundwater model: US Geological Survey software release. Reston, VA: USGS. https://doi.org/10.5066/F7RF5S7G.
- Le Borgne, T., M. Dentz, D. Bolster, J. Carrera, J.-R. de Dreuzy, and P. Davy. 2010. "Non-Fickian mixing: Temporal evolution of the scalar dissipation rate in heterogeneous porous media." Adv. Water Resour. 33 (12): 1468–1475. https://doi.org/10.1016/j.advwatres.2010.08.006.
- Le Borgne, T., M. Dentz, and J. Carrera. 2008a. "Lagrangian statistical model for transport in highly heterogeneous velocity fields." Phys.

- Rev. Lett. 101 (9): 090601. https://doi.org/10.1103/PhysRevLett.101.090601.
- Le Borgne, T., M. Dentz, and J. Carrera. 2008b. "Spatial Markov processes for modeling Lagrangian particle dynamics in heterogeneous porous media." *Phys. Rev. E* 78 (2): 026308. https://doi.org/10.1103/PhysRevE .78.026308.
- Le Borgne, T., M. Dentz, and E. Villermaux. 2013. "Stretching, coalescence, and mixing in porous media." *Phys. Rev. Lett.* 110 (20): 204501. https://doi.org/10.1103/PhysRevLett.110.204501.
- Le Borgne, T., T. R. Ginn, and M. Dentz. 2014. "Impact of fluid deformation on mixing-induced chemical reactions in heterogeneous flows." Geophys. Res. Lett. 41 (22): 7898–7906. https://doi.org/10.1002/2014GL062038.
- Lester, D. R., G. Metcalfe, and M. G. Trefry. 2013. "Is chaotic advection inherent to porous media flow?" *Phys. Rev. Lett.* 111 (17): 174101. https://doi.org/10.1103/PhysRevLett.111.174101.
- Lester, D. R., M. Rudman, G. Metcalfe, M. G. Trefry, A. Ord, and B. Hobbs. 2010. "Scalar dispersion in a periodically reoriented potential flow: Acceleration via Lagrangian chaos." *Phys. Rev. E* 81 (4): 046319. https://doi.org/10.1103/PhysRevE.81.046319.
- Mays, D. C., and R. M. Neupauer. 2012. "Plume spreading in groundwater by stretching and folding." *Water Resour. Res.* 48 (7): W07501. https://doi.org/10.1029/2011WR011567.
- Meunier, P., and E. Villermaux. 2010. "The diffusive strip method for scalar mixing in two dimensions." *J. Fluid Mech.* 662 (Nov): 134–172. https://doi.org/10.1017/S0022112010003162.
- Neupauer, R. M., and D. C. Mays. 2015. "Engineered injection and extraction for in situ remediation of sorbing solutes in groundwater." *J. Environ. Eng.* 141 (6): 04014095. https://doi.org/10.1061/(ASCE)EE .1943-7870.0000923.
- Neupauer, R. M., L. J. Sather, D. C. Mays, J. P. Crimaldi, and E. J. Roth. 2020. "Contributions of pore-scale mixing and mechanical dispersion to reaction during active spreading by radial groundwater flow." Water Resour. Res. 56 (7): e2019WR026276. https://doi.org/10.1029/2019WR026276.
- Orfanidis, S. J. 1995. *Introduction to signal processing*. Upper Saddle River, NJ: Prentice-Hall, Inc.
- Ou, J.-J., and W. Ranz. 1983. "Mixing and chemical reactions: A contrast between fast and slow reactions." *Chem. Eng. Sci.* 38 (7): 1005–1013. https://doi.org/10.1016/0009-2509(83)80021-9.
- Perez, L. J., J. Hidalgo, A. Puyguiraud, J. Jiménez-Martínez, and M. Dentz. 2020. "Assessment and prediction of pore-scale reactive mixing from experimental conservative transport data." Water Resour. Res. 56 (6): e2019WR026452. https://doi.org/10.1029/2019WR026452.
- Piscopo, A. N., R. M. Neupauer, and D. C. Mays. 2013. "Engineered injection and extraction to enhance reaction for improved in situ remediation." *Water Resour. Res.* 49 (6): 3618–3625. https://doi.org/10 .1002/wrcr.20209.
- Porta, G. M., S. Chaynikov, J.-F. Thovert, M. Riva, A. Guadagnini, and P. M. Adler. 2013. "Numerical investigation of pore and continuum scale formulations of bimolecular reactive transport in porous media." Adv. Water Resour. 62 (2): 243–253. https://doi.org/10.1016/j.advwatres .2013.09.007.
- Raje, D. S., and V. Kapoor. 2000. "Experimental study of bimolecular reaction kinetics in porous media." *Environ. Sci. Technol.* 34 (7): 1234–1239. https://doi.org/10.1021/es9908669.
- Rodríguez-Escales, P., D. Fernàndez-Garcia, J. Drechsel, A. Folch, and X. Sanchez-Vila. 2017. "Improving degradation of emerging organic compounds by applying chaotic advection in managed aquifer recharge in randomly heterogeneous porous media." Water Resour. Res. 53 (5): 4376–4392. https://doi.org/10.1002/2016WR020333.
- Rolle, M., C. Eberhardt, G. Chiogna, O. A. Cirpka, and P. Grathwohl. 2009. "Enhancement of dilution and transverse reactive mixing in porous media: Experiments and model-based interpretation." *J. Contam. Hydrol.* 110 (3–4): 130–142. https://doi.org/10.1016/j.jconhyd .2009.10.003.
- Salamon, P., D. Fernàndez-Garcia, and J. J. Gómez-Hernández. 2006. "Modeling mass transfer processes using random walk particle

- tracking." Water Resour. Res. 42 (11): W11417. https://doi.org/10.1029/2006WR004927.
- Speetjens, M. F. M., G. Metcalfe, and M. Rudman. 2021. "Lagrangian transport and chaotic advection in three-dimensional laminar flows." *Appl. Mech. Rev.* 73 (3): 1. https://doi.org/10.1115/1.4050701.
- Suthersan, S., C. Divine, and S. Potter. 2009. "Remediating large plumes: Overcoming the scale challenge." *Groundwater Monit. Rem.* 29 (1): 45–50. https://doi.org/10.1111/j.1745-6592.2008.01226.x.
- Suthersan, S., E. Killenbeck, S. Potter, C. Divine, and M. LeFrancois. 2015. "Resurgence of pump and treat solutions: Directed groundwater recirculation." *Groundwater Monit. Rem.* 35 (2): 23–29. https://doi.org/10.1111/gwmr.12114.
- Trefry, M. G., D. R. Lester, G. Metcalfe, A. Ord, and K. Regenauer-Lieb. 2012. "Toward enhanced subsurface intervention methods using chaotic advection." *J. Contam. Hydrol.* 127 (1–4): 15–29. https://doi.org/10 .1016/j.jconhyd.2011.04.006.
- Yoon, Y. E., and F. W. Schwartz. 1999. "Oxidative degradation and kinetics of chlorinated ethylenes by potassium permanganate." *J. Contam. Hydrol.* 37 (3–4): 343–365. https://doi.org/10.1016/S0169-7722 (98)00166-1.
- Zhang, P., S. L. DeVries, A. Dathe, and A. C. Bagtzoglou. 2009. "Enhanced mixing and plume containment in porous media under time-dependent oscillatory flow." *Environ. Sci. Technol.* 43 (16): 6283–6288. https://doi.org/10.1021/es900854r.